Contents lists available at ScienceDirect

Remote Sensing of Environment

Check for updates

Monitoring glacial lake outburst flood susceptibility using Sentinel-1 SAR data, Google Earth Engine, and persistent scatterer interferometry

Sonam Wangchuk [a,c,*], Tobias Bolch [a,*], Benjamin Aubrey Robson [b]

[a] Department of Geography & Sustainable Development, University of St Andrews, St Andrews, UK
[b] Department of Earth Sciences, University of Bergen, Bergen, Norway
[c] Now at the Faculty of Science, Vrije Universiteit Amsterdam, Amsterdam, Netherlands

ARTICLE INFO

ABSTRACT

Continuous monitoring of glacial lakes, their parent glaciers and their surroundings is crucial because possible outbursts of these lakes pose a serious hazard to downstream areas. Ongoing climate change increases the risk of this hazard globally due to recession of glaciers leading to formation and expansion of glacial lakes, and permafrost degradation which impacts the stability of glaciers, slopes and moraines. Here, we demonstrate the capability of our approach for monitoring lake outburst susceptibility using time-series of Sentinel-1 Synthetic Aperture Radar (S-1 SAR) data. We selected Lunana in the Bhutanese Himalayas as an example region as it is highly susceptible to glacial lake outburst floods and suitable baseline data were available. We used Google Earth Engine (GEE) to calculate average radar backscatter intensity (ARBI) of glaciers, lakes, basins, and moraines. To determine the periodicity of the highest and the lowest radar backscatter intensity, we denoised the ARBI data using a Fast Fourier Transform and autocorrelated using a Pearson correlation function. Additionally, we determined glacier melt area, basin melt area, lake area, open water area, and lake ice area using radar back-scatter intensity data. The Persistent Scatterer Interferometry (PSI) technique was used to investigate the stability of moraines and slopes around glacial lakes. The PSI results were qualitatively validated by comparison with high-resolution digital elevation model differencing results. Our approach showed that glaciers and basins in the region underwent seasonal and periodic changes in their radar backscatter intensity related to changes in ice and snow melt. Lakes also showed seasonal changes in their radar backscatter intensity related to the variation of lake ice and open water area, but the radar backscatter intensity change was not periodic. We could also infer lake area change using a time-series radar backscatter intensity data such as the rapid expansion of Bechung Tsho. The PSI analysis showed that all the terminal moraines were stable except Drukchung Tsho. Its terminal moraine showed subsidence at the rate of –5.18 mm/yr. Sidewalls of lakes were also stable with the exception of Lugge Tsho at site 4. Due to the free availability of S-1 SAR data, the efficiency of processing a large amount of imagery within GEE, and the PSI technique, we were able to understand the outburst susceptibility of glacial lakes in the region at great detail. The regular acquisition of S-1 SAR data enables continuous monitoring of glacial lakes. A similar approach and concept can be transferred to any geographic region on earth that shares similar challenges in glacial lake monitoring.

1. Introduction

Glaciers worldwide have been retreating throughout the latter half of the twentieth century due to the increase in global temperature and changes in precipitation. Numerous glacial lakes have formed in their wake across the mountainous areas of the earth during the last decades (How et al., 2021; Miles et al., 2017; Shugar et al., 2020; Wangchuk and Bolch, 2020). This is also true for High Asia, also referred to as the Third Pole, where numerous inventories of glacial lakes exist. For example, Zhang et al. (2015) reported 5701 glacial lakes in the region. An inventory by Wang et al. (2020) reported even more glacial lakes (around 30,000) although the definition of glacial lakes can differ from study to study depending on the interpretation of their genesis and location (Wangchuk and Bolch, 2020; Zhang et al., 2015). Owing to cloud computing technology, an inventory of glacial lakes, created using Landsat images and the NDWI composite maps, even at the global scale

---

* Corresponding authors.
  E-mail addresses: s.wangchuk@vu.nl (S. Wangchuk), tobias.bolch@st-andrews.ac.uk (T. Bolch).

is now available (Shugar et al., 2020), although the number and area of glacial lakes could have underestimated because of challenges faced in lake mapping such as cloud cover, shadows and lake turbidity (How et al., 2021; Wangchuk and Bolch, 2020).

Some glacial lakes can be potentially dangerous as they are undergoing a sustained increase in the lake volume and thawing of their surrounding permafrost due to the glacier recession and rising temperature. Systematic hazard assessment studies that considered multiple parameters that could trigger glacial lake outburst floods (GLOF) have reported many dangerous glacial lakes around the world. In the southeastern Tibetan Plateau, 10 out of 78 investigated glacial lakes were identified as potentially dangerous (Wang et al., 2012). In the Northern Tien Shan, out of 132 glacial lakes surveyed 47 were found to have a medium to a high degree of danger (Bolch et al., 2011). In Uzbekistan, 15% of 242 glacial lakes were found to be dangerous (Petrov et al., 2017). Across the entire Tibetan Plateau, out of 1291 glacial lakes subjected to an objective hazard analysis around 16% (206 glacial lakes) exhibited a threat to downstream settlements (Allen et al., 2019). Similarly, in the Bolivian Andes, out of 137 glacial lakes investigated, 25 lakes were found to be dangerous (Cook et al., 2016).

GLOFs have resulted in the direst loss of lives and properties in many parts of the world (Carrivick and Tweed, 2016). For example, in the Chileno Valley (Wilson et al., 2019), Tien Shan (Narama et al., 2010), Bhutanese Himalayas (Gurung et al., 2017; Watanbe and Rothacher, 1996), and Nyainqentanglha (Zheng et al., 2021). This is a particular problem in High Mountain Asia, where GLOFs have killed more than 6300 people since the 1500s. The main trigger of a GLOF is the failure of moraine dams. Moraine dam failure can be triggered by the degradation of ice-cored moraine and permafrost due to the rising temperature, the growing hydrostatic pressure due to a lake expansion, and the tsunami-like wave from detached mass (e.g., ice, rock, landslide) from creeping lake sidewalls (Byers et al., 2019; Westoby et al., 2014; Worni et al., 2012). An excessive amount of rainfall in a basin and glacier melting can also trigger lake outbursts because the disintegration of ice within the moraine and rising hydrostatic pressure undermine its long-term structural integrity (Richardson and Reynolds, 2000; Rounce et al., 2016). Although the frequency of GLOFs in the Himalayas has remained unchanged (Veh et al., 2019), it is likely to increase in the future due to climate change and resulting moraine and slope instability (Harrison et al., 2018; Clague and Evans, 2000). Sometimes a GLOF from a lake can occur multiple times from the same lake (e.g., Dussaillant et al., 2010; Kropacek et al., 2015) thus requiring frequent monitoring.

The triggers of GLOFs such as the failure of ice-cored moraines and creeping slopes around the lakes can be monitored using satellite technology and field-based observations. A modelled permafrost map was used as a proxy to infer the presence of ice within a moraine (Bolch et al., 2011). Other studies inferred the presence of ice by analysing the morphology of the moraine using high-resolution satellite imagery (McKillop and Clague, 2007). Field-based investigations of ice cliffs and karst are also used (Richardson and Reynolds, 2000). Additionally, studies have analysed the evolution of lake outlet channels and the presence of ponds on the moraine using Google Earth images and high-resolution satellite imagery (Rounce et al., 2016). The above approaches are appropriate to usebut they can be expensive, subjective, and error-prone, and cover only a few lakes at a time. Similarly, the likelihood of a landslide or avalanche entering a lake is assessed by analysing the characteristics of slopes and glaciers around the lake using digital elevation models (DEMs) and high-resolution images (Huggel et al., 2002; Bolch et al., 2011). Steeper slopes (greater than 30 degrees) are susceptible to failure during earthquakes and the lakes surrounded by the steeper slopes are usually categorized as high-risk lakes (Rounce et al., 2016; Kargel et al., 2016). However, the use of slope alone can only provide snapshot information about the terrain without motion components. The other means to assess the presence of subsurface ice and slope instability is to use an interferometric technique (InSAR) because it can cover multiple moraines and slopes simultaneously and

measure movements up to millimetre accuracy.

The InSAR technique in general can measure the deformation in a line of sight direction by differencing the phase information between two images acquired at two different times but from nearly the same position. Ideally, the classical InSAR technique performs accurately when scattering features on the earth surface remain nearly the same between image acquisitions. However, performing classical InSAR in glacial and periglacial environments can be challenging as the surface characteristics constantly change due to snowfall, erosion, and groundwater level fluctuations. Additionally, changing atmospheric condition limits the accuracy of InSAR. Therefore, the PSI technique is highly suitable for our study because the technique uses only stable scatterers (thus persistent) from a time-series of interferograms to measure ground deformation at the original resolution of SAR satellite data. Previously, the InSAR and PSI techniques were used to measure crustal deformation and landslide activities (Hooper et al., 2012; Tofani et al., 2013) and slope instabilities in Bhutan (Dini et al., 2019; Scapozza et al., 2019).

The main aim of the study is to demonstrate the capabilities of S-1 SAR backscatter intensity data, GEE, and the PSI technique for monitoring glacial lakes and their outburst susceptibility. We exemplify our study in the Lunana region of the Bhutanese Himalayas and shed light on the characteristics of glacial lakes and their surroundings (glacier melt, basin melt, lake area, open water area, lake ice area, moraine stability, and slope stability) that can be quantitatively monitored with a high repeat cycle.

2. Study area

The case study was undertaken in Lunana, the northernmost region of the Bhutanese Himalayas which is highly susceptible to GLOF events and major downstream impacts (Fig. 1). The area has five valley glaciers namely Bechung, Raphstreng, Thorthomi, Lugge, and Drukchung, originating from the Table Mountains (the main snow accumulation area for the glaciers) that separates Tibet (China) to the north and Bhutan to the south. The meltwater originating from these glaciers flows directly into Pho Chu (Chu = river) that drains into Punatshang Chu and finally into the Brahmaputra river that drains into the Bay of Bengal. Glaciers in the regions are mainly fed by the snow avalanches from the steeper south-facing slopes of the Table Mountains. The equilibrium line altitude (ELA) of Bechung and Raphstreng glaciers, based on Sentinel-2 imagery acquired on 23 August 2019, are 6710 m and 6423 m, respectively. Thorthomi glacier has three tributaries where the main tributary is directly connected to the accumulation zone and two small tributaries are fed by a snow avalanche. The ELA lies around 6129 m. Lugge glacier is directly connected to the accumulation zone and the ELA is around 5780 m. Both Thorthomi and Lugge glaciers are undergoing significant negative surface elevation change: at a mean rate of 1.4 ma^{-1} and 4.67 ma^{-1}, respectively (Tsutaki et al., 2019).

All the glaciers are debris-covered in the lower parts of the ablation zone and terminate into well-developed proglacial lakes (see Table 1 for their area in 2019). Supraglacial ponds are visible on the debris-covered surfaces of the glaciers as of Sentinel-2 imagery (08 August 2019). In addition, Thorthomi and Lugge glaciers have debris-free mantled ice along a glacier flowline that directly connect to its proglacial lake. Bechung Tsho (Tsho = lake) is the smallest of four lakes considered for the study. It initially appeared as supraglacial ponds in the 1990s (Mahagaonkar et al., 2017). Currently, it is an actively developing proglacial lake that mainly extends northwards; debris-covered ice of Bechung glacier calves into the lake. Raphstreng Tsho on the other hand is a fully formed proglacial lake with a maximum bathymetric depth of 110 m and an estimated volume of around 55×10^6 m^3 (Komori, 2008; NCHM, 2019). Although it is surrounded by steep terrain and an actively flowing glacier, no previous outburst has been reported from this lake.

Thorthomi Tsho is of particular interest because it was formed approximately at the same time as Raphstreng Tsho (Table 1), but it
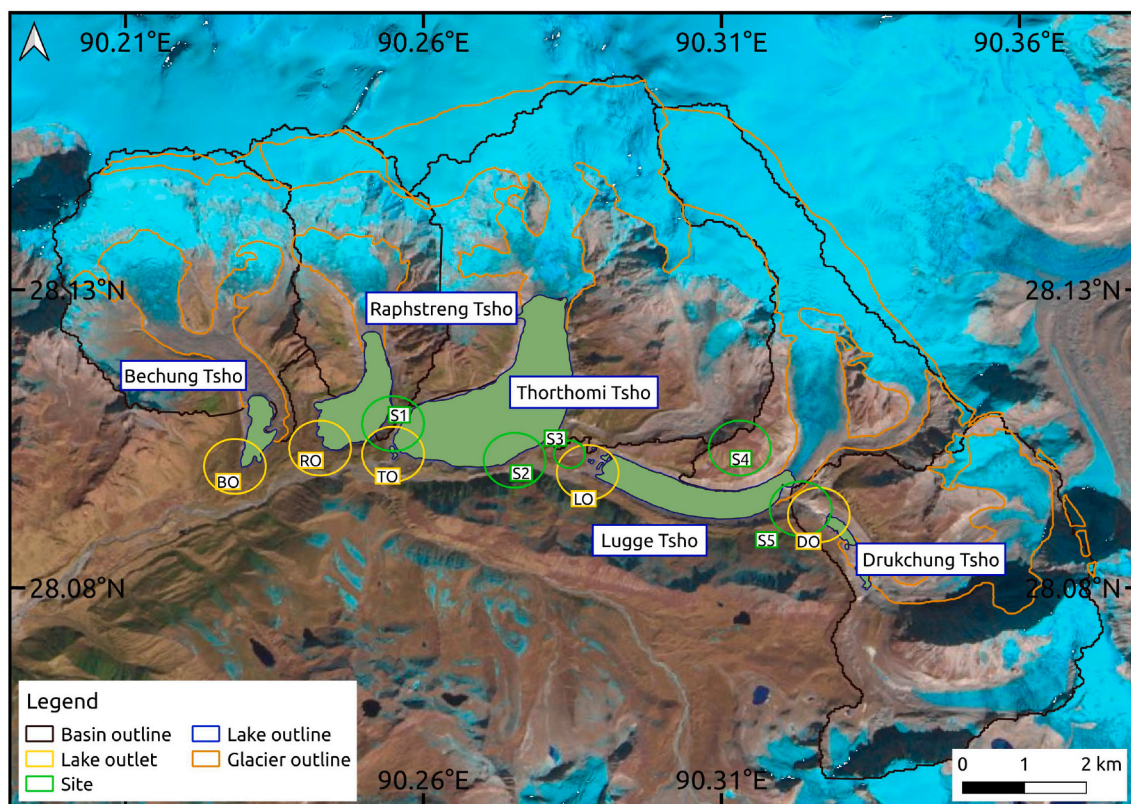
Fig. 1. Study area, Lunana, the Bhutanese Himalayas. The yellow circles are the outlets of lakes, Bechung outlet (BO), Raphstreng outlet (RO) and so on with a radius of 500 and used to analyse the deformation rate and density of persistent scatterers. The green circles show the area of sites, site 1 (S1), site 2 (S2) and so on, with a radius of 500 m except S3 with 250 m and used to analyse the same. S1 is a narrow lateral moraine that separates Raphstreng Tsho and Thorthomi Tsho. S2 is also a lateral moraine of Thorthomi Tsho. S3 is a terminal moraine of Lugge Tsho. S4 is likely a plateaued arête of the Lugge glacier which is now one of the mass movement zones of Lugge Tsho. S5 is a terminal moraine of Drukchung Tsho. Background is a false color composite Sentinel-2 imagery acquired on 25 November 2020. (For interpretation of the references to color in this figure legend, the reader is referred to the web version of this article.)

Table 1
List of glacial lakes in Lunana, the Bhutanese Himalayas, used for a case study. The initial lake area was taken from and manually updated using the Sentinel-1 imagery acquired on 08 August 2019.

Sl. no	Lake name	Area (km^2)	Latitude, Longitude	Formation year	Characteristics	Previous outburst record
1	Bechung Tsho	0.42	28.103, 90.231	1990s	Ice-contact proglacial lake with a parent glacier (clean + debris) of 4.83 km^2.	No
2	Raphstreng Tsho	1.36	28.107, 90.247	Early 1950s	Fully formed ice-contact proglacial lake with a parent glacier (clean + debris) of 3.50 km^2.	No
3	Thorthomi Tsho	4.41	28.108, 90.272	Mid 1950s	Ice-contact proglacial lake with a parent glacier (clean + debris) of 10.80 km^2. Contains numerous floating icebergs.	2019 (Kuensel, 2019)
4	Lugge Tsho	1.62	28.093, 90.299	Mid 1960s	Fully formed ice-contact proglacial lake with a parent glacier (clean + debris) of 10.69 km^2. Highly turbid glacial lake.	1994 (Watanbe and Rothacher, 1996)
5	Drukchung Tsho	0.15	28.087, 90.326	1970s	Proglacial lake with a parent glacier size of 4.54 km^2	Yes (drained by the first week of July 2019)

contains a huge amount of icebergs on the lake surface and its identification in satellite imagery is challenging even visually. As scientific investigations found that this lake could potentially and catastrophically burst into Raphstreng Tsho by undermining the 30–50 m lateral moraine that separates these two lakes, lake level lowering activity was conducted between 2008 and 2012, which lowered the lake level by 5 m (Singh, 2009). However, a minor outburst on 20 June 2019 from a subsidiary lake located at the outlet caused downstream panic, destroyed an automatic weather station, and a few cantilever bridges downstream (Kuensel, 2019). The cause and processes of the outburst deserve detailed scientific investigations although the local media reported that excessive melting of glaciers due to rising temperature triggered the outburst. Similarly, Lugge Tsho located on the right side of

it has a record of previous partial outburst in 1994 due to a lateral moraine failure. It released a lake volume of 17 million cubic meters (Fujita et al., 2008) which killed 21 persons and destroyed agricultural land and infrastructure located almost 70–80 km downstream (Maurer et al., 2020; Watanbe and Rothacher, 1996). As of 2019 the surface area of the lake was 1.5 km^2 (Wangchuk and Bolch, 2020). The maximum depth and volume of the lake were 97 m and 65 × 10^6 m^3 as of 2011, respectively (NCHM, 2019). The lake has a narrow outlet with active landslide activity at moraines but lacks a steep lakefront area (Fujita et al., 2013).

3. Data and methods

3.1. Zonation of glacial landforms for monitoring

Glacial landforms in the study area were divided into zones: glacier, lake, basin, moraine, and slope to be used as Regions of Interest (ROI) for generating a respective time-series radar backscatter intensity data within GEE. We obtained glacier polygons from the Japan Aerospace Exploration Agency (Nagai et al., 2016, 2017). Since these glacier outlines were digitised using the Advanced Land Observing Satellite imagery obtained between 2006 and 2011, outlines (especially at the glacier tongue) were manually updated using a false-color composite image of S-2 (08 August 2019) and greyscale image of S-1 for the recent outline. Glacial lake outlines were used from Wangchuk and Bolch (2020) except for Thorthomi Tsho which was manually digitised using the same images mentioned above. An automatic delineation of Thorthomi Tsho was not possible using S-1 or S-2 images as it contained numerous icebergs on its surface. The boundary of a lake basin, moraine, and slope was manually delineated within QGIS software using a 30 m Shuttle Radar Topography Mission (SRTM) V3 DEM and sub-metre resolution images available for visualisation through Google Earth (Fig. 1).

3.2. Data availability and Google Earth Engine

We used Level-1 high-resolution S-1 SAR datasets, in particular Interferometric Wide swath (IW) acquisition mode datasets, for monitoring glacier melt area, lake area, open water area, lake ice area, moraine stability, and slope stability within the ROIs generated in Section 3.1. They were acquired by the Copernicus Sentinel-1A and -1B satellites carrying a C-band (5.54 cm wavelength) SAR instrument. The instrument supports a single band polarisation (HH or VV) and a dual band polarisation (HH + HV or VV + VH) and acquires images all-weather, day and night. We used VV polarised band as the coherence and backscatter intensity of VV signal is superior that VH signal in the study area (Wangchuk et al., 2019). The Level-1 datasets can be of two types: Ground Range Detected (GRD) and Single Look Complex (SLC). We used both GRD and SLC products. The GRD datasets have a spatial resolution of 20×22 m in range and azimuth directions and have only amplitude information. Whereas the SLC datasets have a spatial resolution of 2.7×22 m and contain both amplitude and phase information.

The S-1 SAR single look complex (SLC) datasets were accessed using Vertex, the search-and-download client of Alaska Satellite Facility. We used a Vertex baseline tool to identify and select SLC images from the archive. The Vertex baseline tool has the capability to visualise perpendicular and temporal baseline data, allowing only the selection of image pairs that are suitable for interferogram generation. We selected one suitable scene, having the smallest perpendicular baseline value with respect to a master image, from each month and year (May–October and 2017–2019) of the summer and autumn seasons, when seasonal snowfall in images was expected to be minimal. The selected scene was also assumed to be representative of other available scenes for a month in terms of presence of persistent scatterers. Therefore, both the number of minimum scenes required for the PSI (15 scenes) and the reduction of computation time were satisfied.

Google Earth Engine (GEE) is a freely available cloud computing platform provided by Google for a global-scale geospatial data analysis (Gorelick et al., 2017). We used the Earth Engine Code Editor, a web-based integrated development environment for scripting and executing codes, and to interact with the platform and data. The Level-1 high-resolution S-1 SAR GRD datasets within GEE are calibrated, orthorectified, and log-scaled products with a pixel size of 10 m. Terrain correction of datasets was performed using the SRTM 30 m DEM.

3.3. Retrieval of radar backscatter intensity time-series data

We created a GEE image collection object of Level-1 S-1 GRD products using the Earth Engine asset ID: 'COPERNICUS/S1_GRD'. We filtered images within the image collection object using ROI and other attributes of S-1 SAR data such as a date range of image acquisition (03-04-2014: 31-12-2020), polarisation (VV), instrument mode (IW), relative orbit number (114/150), and orbit pass (ascending/descending). Finally, images within the image collection object were sorted from the oldest to the latest dates of image acquisitions. The total number of scenes overlapping all of our ROIs was 340 (Fig. S1).

A mean radar backscatter intensity, along with their acquisition timestamps, was determined for each S-1 SAR image in the image collection object and for each ROI. We visualised the time-seres data within Code Editor to assess the data quality before exporting it as a comma-separated values file to be analysed and visualised in Python 3.

3.4. Spectral analysis: discrete Fourier transform on time-series data

In order to automatically determine periodicity of the highest and the lowest radar backscatter intensity in a time-series radar backscatter intensity data generated in Section 3.3, we used NumPy's 'fft' function to compute one-dimensional discrete Fourier transform (DFT) using the fast Fourier transform (FFT) algorithm. This approach decomposed a time domain signal into a frequency domain signal of increasing frequency (Fourier Coefficients) where a sum of frequency components would recover an original signal. The frequency content of the signal was calculated at a sampling frequency (Hz) of 6.4 days as it best approximated the raw signal (Fig. 2). We also calculated a power spectral density (PSD) to determine the signal power content at each frequency (W/Hz). The frequency component containing the maximum PSD was extracted by thresholding the PSD data. We performed an inverse FFT on the resulting signal to produce a denoised time domain signal and applied a Pearson autocorrelation function (ACF) to determine autocorrelation coefficients (ACC). We used SciPy's 'find_peaks' function to locate index positions of ACF coefficients with a local maxima and minima. The index position of an integer was multiplied by sampling frequency and differenced to acquire periodicity (Fig. 2).

3.5. Identification of melt pixels

To infer melting pixels of glaciers, basins, and moraines surfaces, we manually identified four land cover classes relatively with a flat topography using Google Earth images: alluvial soil, debris-covered ice, clean ice, and percolation facies. The flat area was defined as the region associated with an average slope of less than 10 degrees. The flat area was assumed to be associated with no or minimal radar image artifacts and similar incidence angle, therefore, reliable for identification of thresholds. The following steps were employed: (1) we extracted an average radar backscatter intensity data of four land cover classes using GEE; (2) we removed outliers present in the data using Tukey's method (Tukey et al., 1977). This method eliminated data points greater than 1.5 times the interquartile range from the quartiles (i.e., the data points either below Q1-1.5IQR, or above Q3+1.5IQR, where Q1, Q3 and IQR are first quartile, second quartile, and interquartile range); (3) we smoothed the data using a moving average technique with the moving window of three samples; (4) we decomposed the data into its trend, seasonal and residual components using a time-series additive model (Table 2); and (5) we separated the trend and seasonal components and calculated their average values. For the seasonal component, zero was used as the reference value to separate positive and negative amplitude values. All these steps were employed for both ascending and descending data, respectively, thus allowing us to compare their differences in their strengths and variations of radar backscatter intensity across four land cover classes to derive respective thresholds (Table 2).

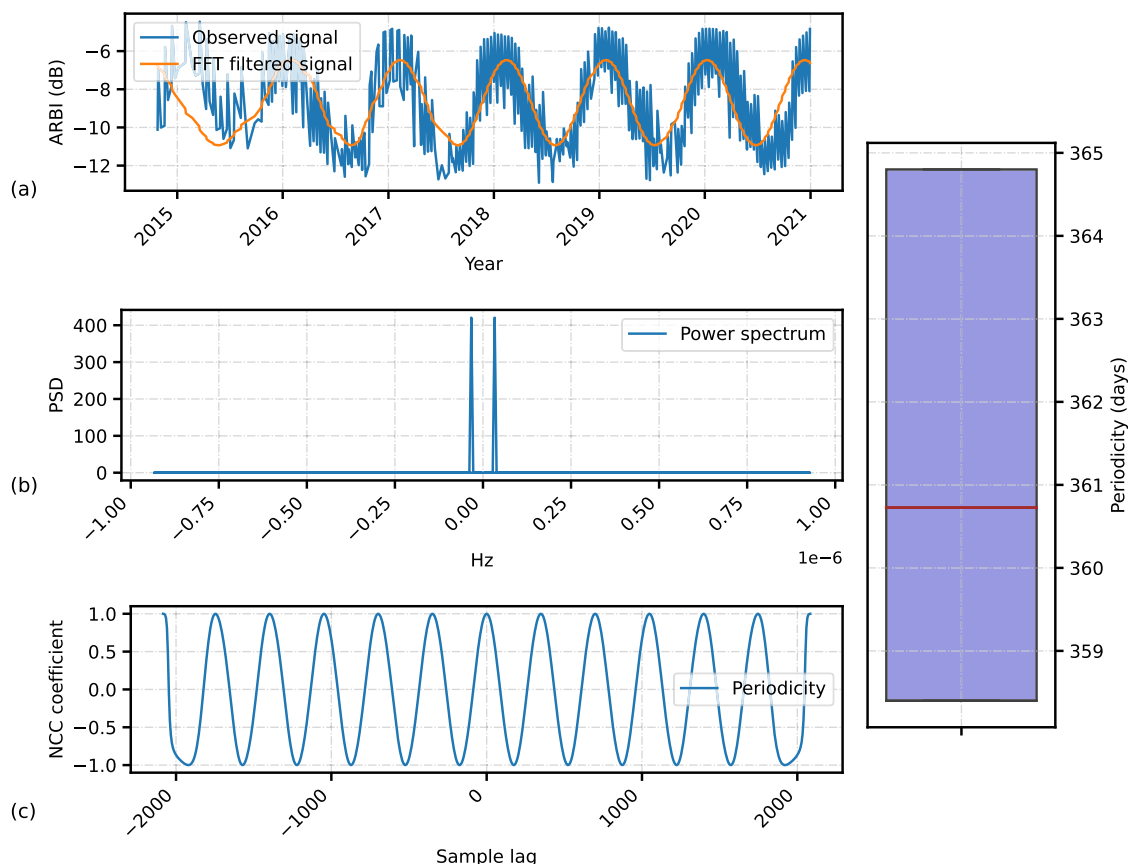Following the above steps and using the information (Table 2),

Fig. 2. (a) Example of an average radar backscatter intensity (ARBI) and the fast Fourier transform (FFT) filtered signal of a glacier surface. (b) Power spectrum of the ARBI. (c) Normalized cross correlation (NCC) sequence of the FFT filtered signal. (d) Periodicity of the highest and the lowest ARBI of the glacier surface with the periodicity of around 360.9 days (red line). (For interpretation of the references to color in this figure legend, the reader is referred to the web version of this article.)

Table 2
Strengths and variations of the radar backscatter between ascending and descending passes and amongst four land cover classes derived from the time-series SAR images available within GEE and relatively at a flat topography.

Sl. no	Land cover class	Ascending trend avg. (dB)	Ascending seasonal amplitude avg. (dB) (+ve avg.| –ve avg.)	Descending Trend avg. (dB)	Descending seasonal amplitude avg. (dB) (+ve avg.| –ve avg.)
1	Alluvial soil	–13.78	1.32|–0.88	–14.45	0.96|–0.97
2	Clean ice	–12.12	0.27|–0.31	–11.83	0.52|–0.84
3	Debris covered ice	–7	0.41|–0.25	–7.08	0.52|–0.59
4	Percolation zone	–6.53	0.25|–0.29	–4.56	0.34|–0.40

thresholds for identifying layover and shadow pixels were defined to be 0 dB as the upper limit and –20 dB as the lower limit. The pixels with the radar backscatter intensity value greater than zero and smaller than –20 dB were removed from the image considering them as image artifacts from layover and shadows. We identified the upper limit threshold for identifying melt pixels as –5.89 dB using the percolation facies statistics. In the percolation zone, the presence of ice pipes and lenses can substantially increase radar backscatter intensity (Partington, 1998). In particular, we averaged the values of the trend and seasonal components (considered only negative amplitude values) of ascending and descending pass (Table 2) to determine the threshold. Also, we determined –17 dB as the lower limit threshold, using open water area

statistics, for identifying melt pixels. The thresholds for obtaining lake area, lake ice area, and open water area were determined by interpreting time-series radar backscatter intensity data (Table 3).

Having determined the thresholds, we followed the approach described in Section 3.3, but to extract a time series data of melting pixels for each ROI (i.e., glaciers, basins, and moraines, lakes). We removed outliers present in the data using Tukey's method (Tukey et al., 1977). The number of pixels that were identified as melting pixels was multiplied by its pixel area (10 m x 10 m) to obtain a total melting area. For glaciers, radar backscatter intensity data and melting area data were analysed with respect to a glacier area and elevation taken from the GAMDAM glacier outlines (Nuimura et al., 2015) and the STRM DEM to understand their changes. For glacial lakes, the radar backscatter intensity data, lake ice area data, and open water area data were analysed

Table 3
Thresholds used for extracting overall lake area, open water area and lake ice area. They were defined based on a time-series information of radar backscatter (dB) data.

Sl. no	Lakes	Overall lake area	Open water area	Ice/rough lake
1	Bechung tsho	dB<–10	dB<–17	dB>17 & dB<–10
2	Raphstreng tsho	dB<–10	dB<–17	dB>17 & dB<–10
3	Thorthomi tsho	dB<–8	dB<–17	dB>17 & dB<–8
4	Lugge Tsho	dB<–10	dB<–17	dB>17 & dB<–10
5	Drukchung tsho	dB<–10	dB<–17	dB>17 & dB<–10

with respect to day of year (DOY) to understand their dynamics such as the timing of a peak lake ice formation. We averaged the data points occurring on the same DOY, across multiple years (e.g., 2014–2020), to get a single observation for each DOY.

3.6. Persistent Scatterer Interferometry processing

The Persistent Scatterer Interferometry (PSI) is a time-series InSAR technique used to measure ground movement such as urban subsidence (Blasco et al., 2019), crustal deformation (Hooper et al., 2012), and landslides (Tofani et al., 2013) by using a deformation signal from only persistent scatterers. The high repeat frequency of S-1 data, allowing the multitemporal generation of interferograms, makes PSI a suitable technique for monitoring stability of lake moraines and slopes in the study area. The datasets which were suitable for generating interferograms were accessed as detailed in Section 3.2. We determined a master image for ascending and descending pass datasets such that the dispersion of the perpendicular baseline of slave images with respect to the master image is as low as possible and the modeled coherence of the interferometric stack is maximum. This approach enabled us to select master images acquired on the 24 of July 2018 and 26 of July 2018 for ascending pass and descending pass datasets respectively. We used sub-swath 3 (IW3) and bursts 6 and 7 for the ascending pass datasets and sub-swaths 1 (IW1) and 2 (IW2) and burst 1 and 2 for the descending pass datasets as the images over our study area were described by these properties. The ascending pass datasets were characterised by the absolute maximum perpendicular baseline of 79 m, and the temporal baseline of 456 days and 85 m and 444 days for the descending pass datasets (Fig. 3). We used S-1 precise orbit data (AUX_POEORB) to correct satellite position and velocity information precisely. We co-registered the reference image and secondary image at sub-pixel level accuracy using an enhanced spectral diversity approach (Fattahi et al., 2016). After co-registration, we generated single master differential interferograms (DiffInSAR). In total we generated 17 DiffInSAR from the

ascending pass datasets and 18 from the descending pass datasets (Table 4). We exported the co-registered stacks and DiffInSAR to a Gamma format data so that it can be read by the StaMPS software. We implemented all these pre-processing steps using the 'snap2stamps' software (Blasco et al., 2019). We added additional pre-processing functionalities into the 'snap2stamps' software such as to support Python 3, burst selection within a sub-swath, and concurrent multi-sub-swath processing and sub-swath DiffInSAR merging. The software is available at https://github.com/swangchuk/snap2stampspy3.

We identified persistent scatterers and retrieved their temporal deformation in the line of sight (LOS) direction by using the StaMPS software. We followed the steps 1 through 8 as indicated in the StaMPS manual. The atmospheric phase component in a DiffInSAR was removed using a phase- and topographic-based linear tropospheric correction approach available in the Toolbox for Reducing Atmospheric InSAR Noise (TRAIN) software that can be integrated within the StaMPS software (Bekaert et al., 2015).

Having determined the temporal deformation of the persistent scatterers in the LOS direction for both ascending and descending datasets, we calculated their average rate of LOS deformation with respect to a reference value of a stable area. Although the PSI technique can measure displacement at a millimetre accuracy, as we do not have a ground truth data for the stable area, we have set a high threshold for defining the moving targets. The ground was interpreted to be unstable

Table 4
Attributes of images used for the Persistent Scatterer Interferometry technique.

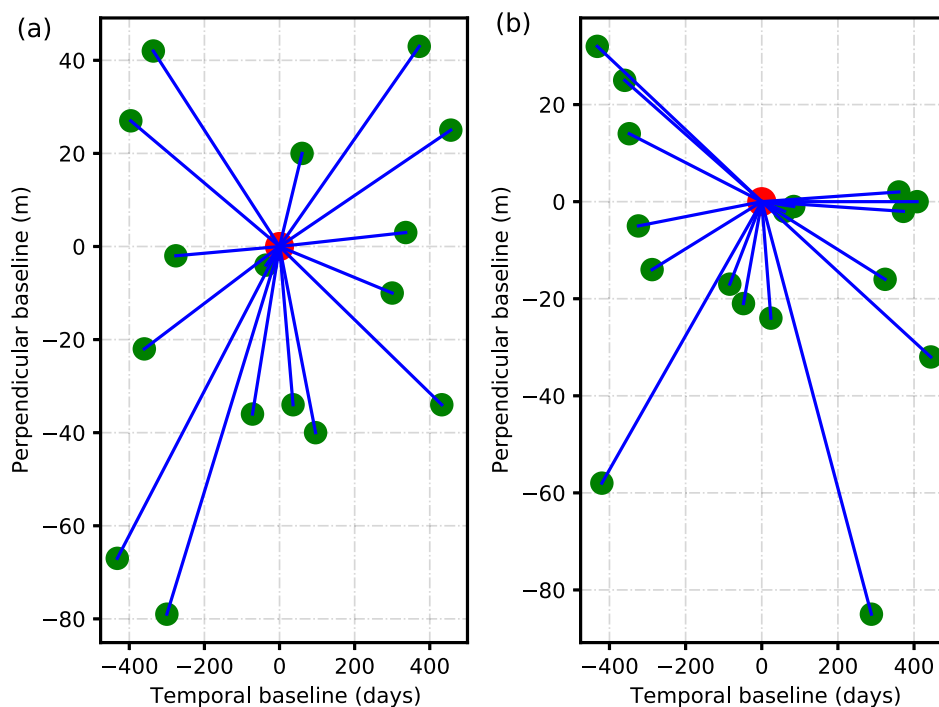| Sl. no	Pass	Orbit number	Sub-swath	Burst	Number of images	Acquisition period
1	Ascending	114	IW3	6,7	17	2017–2019
2	Descending	150	IW2, IW3	1,2	18	2017–2019

Fig. 3. Temporal and perpendicular baselines of interferograms used in this study. The red point represents a single master image and the green points represent slave images for ascending pass (a) and descending pass (b) respectively. The blue lines represent image pairs used to make interferograms for the Persistent Scatterer Interferometry technique. (For interpretation of the references to color in this figure legend, the reader is referred to the web version of this article.)

when the projected deformation rates were outside of the PSI sensitivity range, the value of −1.5 mm/yr for subsidence and 1.5 mm/yr for uplift and same for the east–west motion (Tofani et al., 2013). To increase the number of persistent scatterers, we combined the ascending and descending measurements using a vector-based approach (Foumelis, 2018). We then projected the two LOS measurements as vertical and east–west components under the assumption that there is no motion along the north–south direction as the radar cannot see the motion perpendicular to the LOS direction. We analysed the projected vertical and horizontal deformation and persistent scatterer density at a basin, outlet, and at 5 sites including moraines and slopes. The results of the PSI techniques were qualitatively validated against the DEM differencing results and the field photographs taken in September 2016.

3.7. Digital Elevation Model (DEM) generation and differencing

For validation of the PSI results (Fig. 4), two pairs of stereo satellite imagery, namely a Pleiades image from 2015 and a SPOT 7 image from 2018 were photogrammetrically processed in PCI Geomatica Banff. In both cases, the Rational Polynomial Coefficients (RPCs) were used to solve the exterior orientation. No additional Ground Control Points (GCPs) were used, but approximately 100 tie points were automatically identified for each stereo pair using a fast Fourier transform phase with Blunder Detection (FFTPB) method. The tie points were used to solve the relative orientation and perform a bundle adjustment. Epipolar images were then generated before each DEM was extracted at a 3 m posting using a Semi-Global Matching algorithm, which has been shown to outperform normalised cross-correlation and thereby producing cleaner DEMs (Hirschmüller, 2011).

In order to derive surface elevation changes, the two DEMs were co-registered together using the method set out by Nuth and Kääb (2011) implemented through the Arcpy and Numpy python packages. This method minimises the root mean square slope normalised elevation biases over stable terrain. Lakes and glaciers were masked out from the co-registration, and the process was iterated until the improvement was less than 2%. This resulted in linear shifts in the X, Y, and Z directions of 0.03 m, 2.80 m, and −19.28 m, respectively. Upon examining the elevation biases over stable terrain, no non-linear biases were observed. The surface elevation change raster was filtered using the method proposed by Gardelle et al. (2013) which excludes values greater than three times the standard deviation of the elevation bias over stable terrain.

4. Results

4.1. Glacial lakes and radar backscatter

Glacial lakes in Lunana, the Bhutanese Himalayas, were assessed for their average radar backscatter intensity (ARBI) variations using S-1 time series datasets. All glacial lakes except Raphastreng Tsho exhibited conspicuous seasonal change in their ARBI, however, the change was not periodic. The overall strength of the ARBI was low during summer and high during winter. Lakes also showed higher ARBI variability in winter and spring (less than 6 dB) than in summer and autumn (less than 2 dB). The ARBI trend decreased for Bechung Tsho and increased for
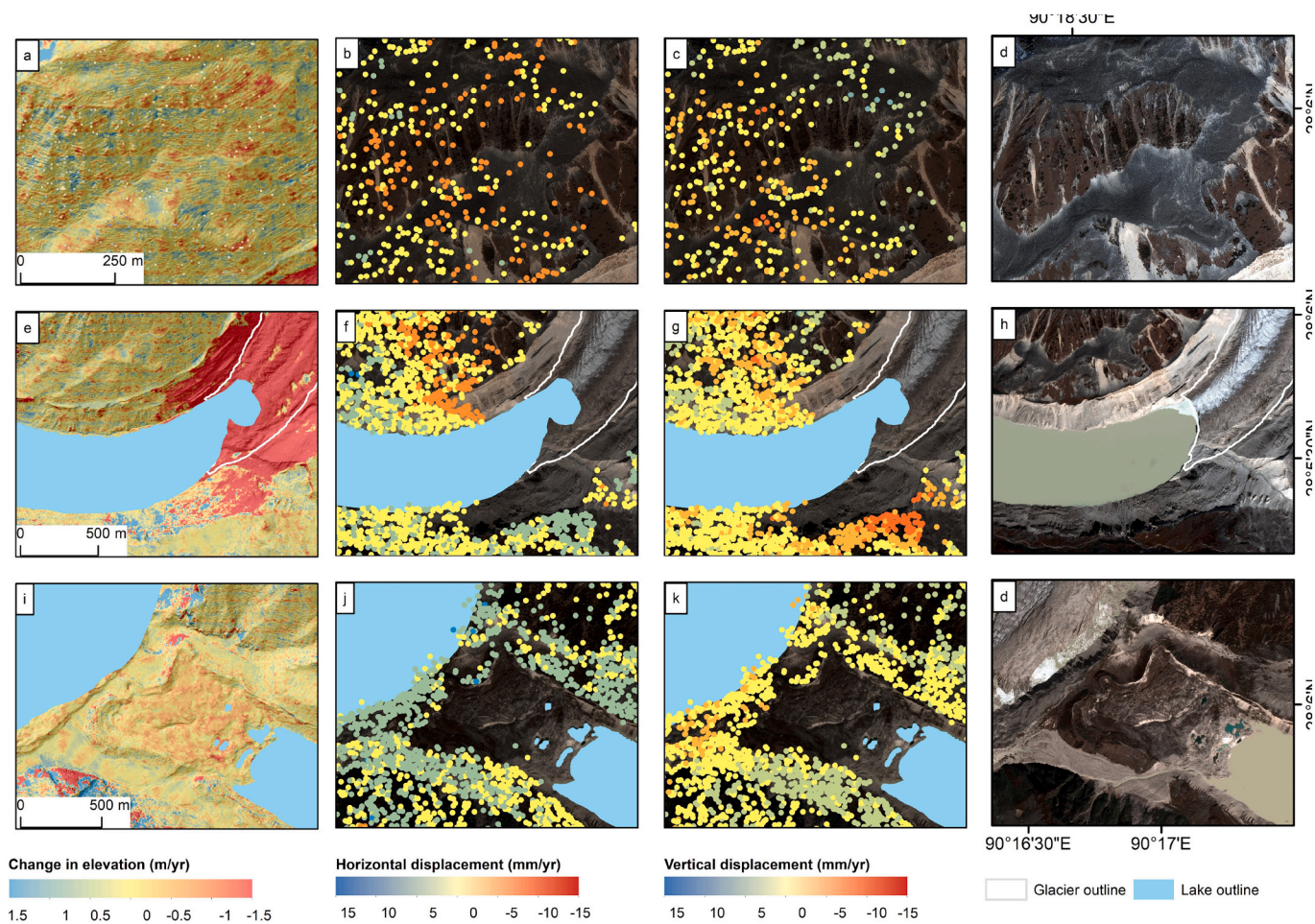

Change in elevation (m/yr)
1.5   1   0.5   0   -0.5   -1   -1.5

Horizontal displacement (mm/yr)
15   10   5   0   -5   -10   -15

Vertical displacement (mm/yr)
15   10   5   0   -5   -10   -15

Glacier outline   Lake outline

Fig. 4. Validation of PSI results with very high-resolution DEM differencing results. Mass movement zone of Lugge Tsho (a, b, c, d), moraines and the terminus of Lugge glacier (e, f, g, h), and moraines of Lugge Tsho (i, j, k, d). The persistent scatterers are missing on the glacier surface. Many persistent scatterers can be seen on the slopes and lateral moraines. The terminal moraine of Lugge Tsho has only few persistent scatterers indicating the presence of subsurface ice.

Drukchung Tsho. At an individual lake level, conspicuous differences in the ARBI were observed. The ARBI peaked in winter for Bechung Tsho, Thorthomi Tsho, and Lugge Tsho for all the analysed years; all four peaks were clearly visible (Fig. 5). Raphstreng Tsho on the other hand had only one peak in 2019. Whereas the peak discontinued for Druk-chung Tsho by mid-2019 thus showing only three peaks priori. The ARBI on Thorthomi Tsho was much higher (less than –8 dB) than other lakes (less than –14 dB) during summer.

4.2. Lake area evolution

Lake area change was monitored using GEE and thresholded time-series S-1 SAR backscatter intensity datasets. Glacial lakes in the region showed sustained growth in their surface area between 2016 and 2020 although the rate of expansion varied amongst lakes. The surface area of Drukchung Tsho increased from 0.29 km^2 in 2016 to 0.41 km^2

(41.38%) in 2020. Raphstreng Tsho (increased from 1.25 km^2 in 2016 to 1.34 in 2020) and Lugge Tsho (increased from 1.49 km^2 in 2016 to 1.60 in 2020) showed a comparable areal expansion: 7.20% and 7.38%, respectively. The area of Bechung Tsho increased from 0.12 km^2 in 2016 to 0.15 km^2 in 2019 (25%) and then decreased to 0.10 km^2 in 2020 (Fig. 5).

4.3. Open water evolution, lake ice and its duration

The open water area of a lake, defined as pixels with a radar back-scatter intensity less than –17 dB, was monitored using GGE and time-series S-1 datasets. The overall trend of open water evolution followed lake area evolution although the open water area was slightly smaller (difference of less than 25% at maximum) than its actual area even during a melt season. A maximum open water area was observed during late spring and summer for all lakes except Thorthomi Tsho. The open
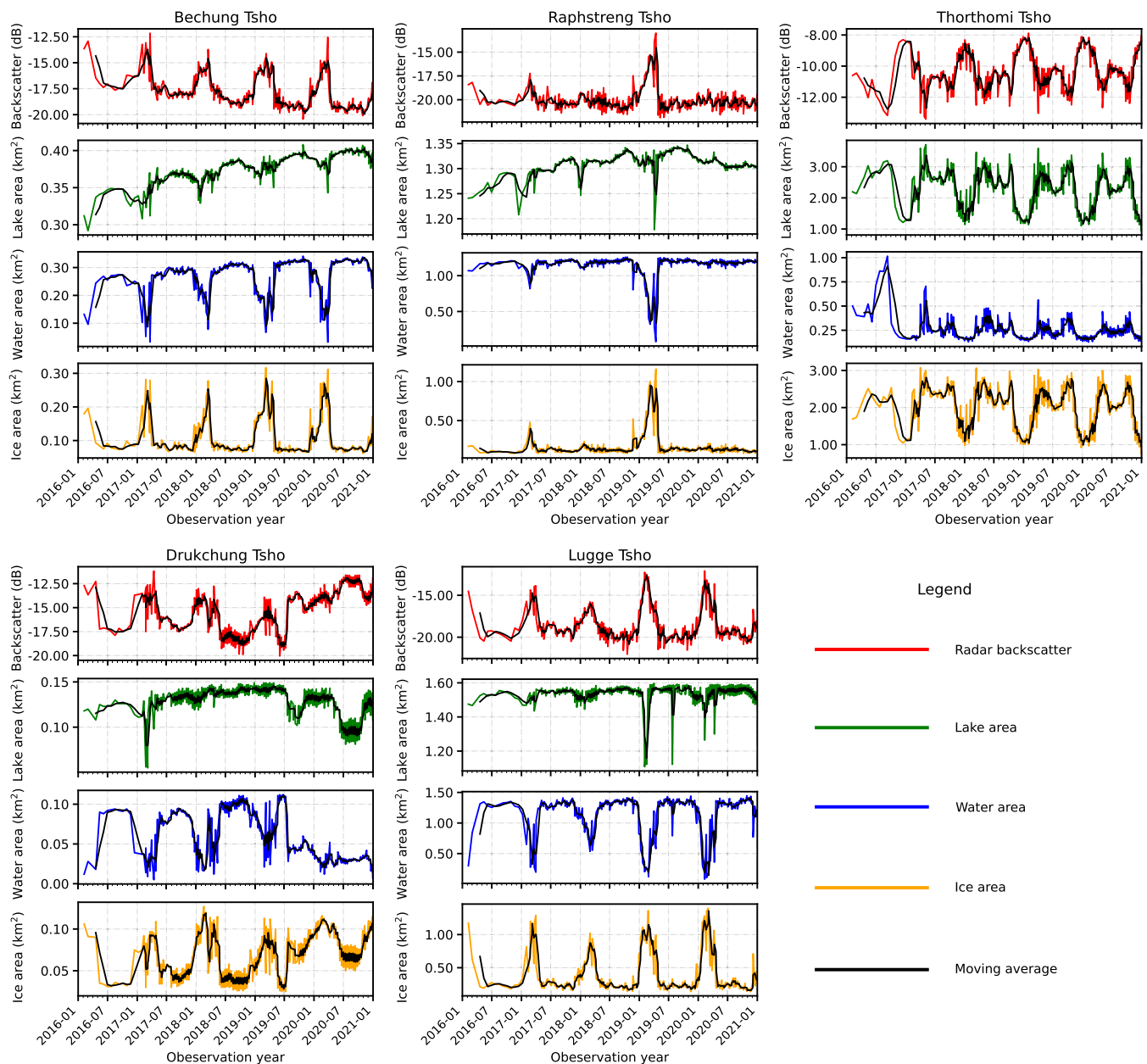

Fig. 5. Variations of the average radar backscatter intensity, lake area, open water area, and ice area of glacial lakes in Lunana, the Bhutanese Himalayas. The spike on lake area for Raphstreng Tsho, around 2019-04-01, could be due to the signal from lake ice which appears like the lake size has reduced.

water area of Thorthomi Tsho substantially decreased from 0.92 km^2 in the summer of 2016 to between 0.18 km^2 and 0.55 km^2 over the subsequent years (Fig. 5).

Glacial lakes were also assessed for their ice area, the time window of their existence, and a peak ice formation using a same approach but with different thresholds. A maximum lake ice area was observed for Bechung Tsho, Lugge Tsho, and Drukchung Tsho during winter as expected. Interannual variations in the lake ice area were also evident. The timing of lake ice duration and peak ice formation differed by around 15 to 35 days (Table 5). In contrast, the formation of lake ice was not so evident for Rasphtreng Tsho (except in the winter of 2018–2019) and Thorthomi Tsho (Fig. 6).

4.4. Glacier surface melting

Glacier melt area was identified when the strength of radar backscatter intensity was between −5.85 dB and −17 dB. All the glaciers in the region were found to be showing seasonal change in their ARBI. The change was periodic with a periodicity of 359–365 days. The strongest median ARBI was observed during winter ($\sim$−5.85 dB) and the weakest median ARBI was observed during summer ($\sim$−14 dB) for all glaciers. The summer median melt area was greater than winter median melt area for Bechung and Raphstreng glaciers. The summer melt duration was also longer (Fig. 7). In contrast, the summer median melt area was smaller than the winter median melt area for Thorthomi, Lugge, and Drukchung glaciers. The overall variation in the median ARBI and melt area showed a clear differences in their strength and area between winter and summer seasons although the range (box whiskers) and interquartile range (box length) of the ARBI and melt area varied amongst glaciers, months, and seasons (Fig. 7).

The surface area of glacier melting was found to be elevation and area dependent, however, the relationship varied between glaciers. For all glaciers, a maximum glacier melting was consistently observed at lower elevations, below 5300 m and greater than 30% (Fig. 11). For Bechung glacier, a maximum glacier area was located below 5400 m elevation bin and the glacier melt area ranged between 38.7% (5400 m) and 67.8% (4300 m). The area of melting at higher elevations (above 6600 m) was greater than lower elevations (above 73%). For Raphstreng glacier, the percentage of melt area was variable at elevations below 5300 m. The percentage of melt area was comparable between lower and higher elevations. The strength of ARBI on both the glaciers increased with decreasing elevations. The Thorthomi glacier also manifested similar behaviour as the Raphstreng glacier in terms of melting area below 5600 m. A maximum glacier area was found between 6000 m and 6500 m with 40 to 50% of its area undergoing melting. Reduced melt area, less than 34.6%, was observed above 6500 m although the glacier area was small (less than 0.35 km^2). The strength of ARBI remained fairly constant between 4500 and 5900 m and steadily increased at elevations higher than 6100 m. The Lugge glacier had a similar glacier area distribution as the Thorthomi glacier, but the trend

of melting area at lower and higher elevations was like the Bechung and Thorthomi glaciers, respectively. The Drukchung glacier underwent intensive melting (greater than 61.8%) below 5100 m compared to higher elevations. Most of its glacier area was found between 4800 m and 5500 m with a melt rate of 45.5 and 81.7%. The median ARBI of glaciers was similar amongst elevation bins and glaciers although the range and interquartile range values varied. The median glacier melt and the variability of other box plot statistics were related to glacier size at each elevation bin, which also differed amongst glaciers. A high variability in glacier melt area was observed especially in the accumulation region of glaciers (Fig. 8).

4.5. Basin-level melting

The basin level melting included only those pixels affected by glacier melt, snow melt, and soil with high moisture. The changes in a basin-level melting area and the ARBI were both seasonal and periodic. The maximum ARBI was observed during winter and spring and the minimum was observed during summer and autumn across all the basins. The ARBI was highly variable throughout the year for the Bechung, Drukchung, and Thorthomi basins. The range of ARBI variability was narrower for the Raphstreng and Lugge basins. The trend of melting was not consistent across basins in contrast to the ARBI. For the Bechung and Raphstreng basins, the summer melt area was greater than the winter melt area and vice versa for the Thorthomi, Lugge, and Drukchung basins. The summer and autumn melt duration for the latter ranged between 170 and 280 DOY. The highest melt area variability was observed at the Thorthomi basin (2–3 km^2) followed by the Bechung and Raphstreng basins (1–2 km^2). The Lugge and Drukchung basins showed less variability in the melt area (Fig. S5).

4.6. Characteristics of melting and radar backscatter at moraines

The characteristics of ARBI and melting were analysed at the terminal moraine, lake outlet, and lateral moraine of Raphstreng Tsho. Particularly, the lateral moraine (between Raphstreng and Thorthomi Tsho and around 30–45 m in width) is susceptible to breach due to the sustained increase in the volume of Thorthomi Tsho and a hydrostatic pressure. Both the ARBI and melting area at the terminal moraine and lake outlet showed their seasonal change. A stronger ARBI was eminent during summer compared to the ARBI during winter, spring, and autumn. A reduction in the melting area was found during summer and the trend remained consistent throughout the entire observation period (2014–2021). The lateral moraine did not show any seasonal change in the ARBI. Instead, a wide range of ARBI (5–15 dB) was observed. These observations were further supported by the analysis of the time-series data in the DOY format. An increase in the ARBI was prominent during summer, peaking at around the 170–220 DOY. At the same DOY range, a reduction in the melt area was observed at the terminal moraine and lake outlet. The lateral moraine showed no deducible variation in the ARBI and the melt area (Fig. S6).

4.7. Persistent scatterers and their deformation rate

The deformation rate of persistent scatterers was analysed at the basins, lake outlets, and ROIs. The median deformation rate at the basins was all within the PSI sensitivity range including outliers (outliers represent persistent scatterers indicating high deformation rates). Only Drukchung's outlet was found to be unstable amongst the terminal moraines/lake outlets as it had higher median deformation value and greater range (long whiskers) and some outliers with relatively high values compared to the datasets of other lake outlets. Also, only the sites 4 and 5 showed a higher instability amongst 5 ROIs analysed (Table 6). Overall, in all the basins, outlets, and sites, a greater range of deformation and outliers, outside of the range of the PSI sensitivity, were observed indicating substantial deformation (Figs. 9 and 10).
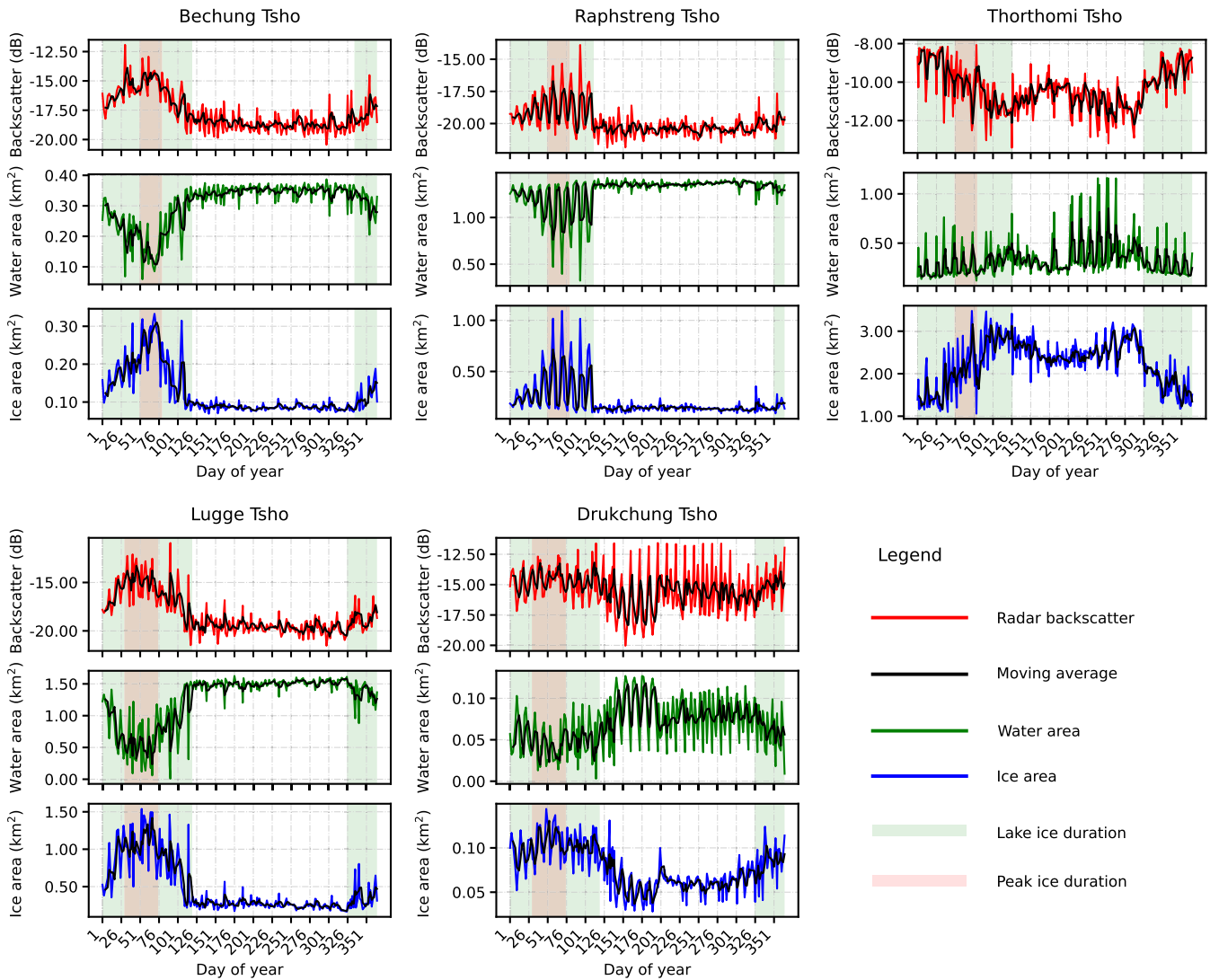
Table 5
Maximum area of lake ice and the duration of lake ice and peak ice formation against DOY. The question mark represents ambiguous lake ice duration and its area.

Sl. no	Lakes	Max ice area (km^2)	Lake ice duration	Peak ice duration
1	Bechung Tsho	0.33	Dec 1 – April 30	Feb 20 – Mar 20
2	Raphstreng Tsho	1.1	Dec 15 – April 20	Feb 20 – Mar 20
3	Thorthomi Tsho	?	Oct 27 – May 5?	Feb 20 – Mar 20?
4	Lugge Tsho	1.34	Nov 20 – April 30	Jan 30 – Mar 15
5	Drukchung Tsho	0.14	Nov 20 – April 30.	Jan 30 – Mar 15

Fig. 6. Average radar backscatter intensity, open water area and lake ice area of glacial lakes with respect to DOY (2016–2020).

5. Discussion

5.1. Monitoring glacial lakes

In this study, five lakes in Lunana were used as experimental lakes for monitoring their outburst susceptibility using S-1 SAR data and GEE. An ABRI of a lake, lake area, open water area, lake ice area, and freezing and thawing of lake ice were monitored at a 6-day interval. The minimum ARBI from the lake surface during late spring, summer, and autumn was mainly attributed to the radar return from an open water surface. The open water surface acts as a smooth surface. As a result, the intensity of radar backscatter appears low irrespective of a lake colour or turbidity, except when the lake surface is affected by wind generated currents (Wangchuk et al., 2019; Strozzi et al., 2012). The lake containing icebergs on its surface can also alter the radar backscatter intensity. For instance, the strength of ARBI on Thorthomi Tsho was higher than the neighbouring lakes, which can be attributed to the dominance of radar return from icebergs. The above findings also support the earlier observation that lakes in the Himalayas undergo seasonal change in their state (Strozzi et al., 2012). Furthermore, the likelihood of occurrence of GLOFs during melt seasons is convincing and consistent with the previous observations (Veh et al., 2019).

An increase in the strength of radar return during winter could be due to the freezing of a lake surface. Thickening of lake ice greater than the penetration depth of the radar can result in a volume scattering from lake ice thereby increasing the strength of the radar return. A further argument for the change in the state of lake surface can be supported by the area of open water area and ice area variations. As expected, the ice area was at a maximum in winter and at a minimum in summer and vice versa for the open water surface area. Likewise, a normal pattern of highs and lows (like a wave) in the backscatter intensity can be expected for most lakes in the Himalayas indicating freezing and thawing of lake. Additionally, our findings suggest that the seasonal change in the state of smaller lakes can be studied in addition to the larger endorheic and exorheic lakes in the Tibetan Plateau (Zhang et al., 2020).

Our ability to monitor freeze-thaw cycle of remote glacial lakes using a time-series ARBI is significant because any deviation from a known pattern of the ARBI would indicate different properties of a lake. For example, our analysis highlighted that Raphstreng Tsho does not undergo complete freezing during winter, which we attributed to the depth of the lake. According to the NCHM (2019) and Komori (2008), it is one of the deepest and fully developed lakes in the region. As such the Raphstreng Tsho could be still dangerous even in winter. In the case of Drukchung Tsho, a change in the ARBI was due to the reduction of its open water area because of its drainage on the first week of July 2019. Although the flooding because of this breach has not been felt
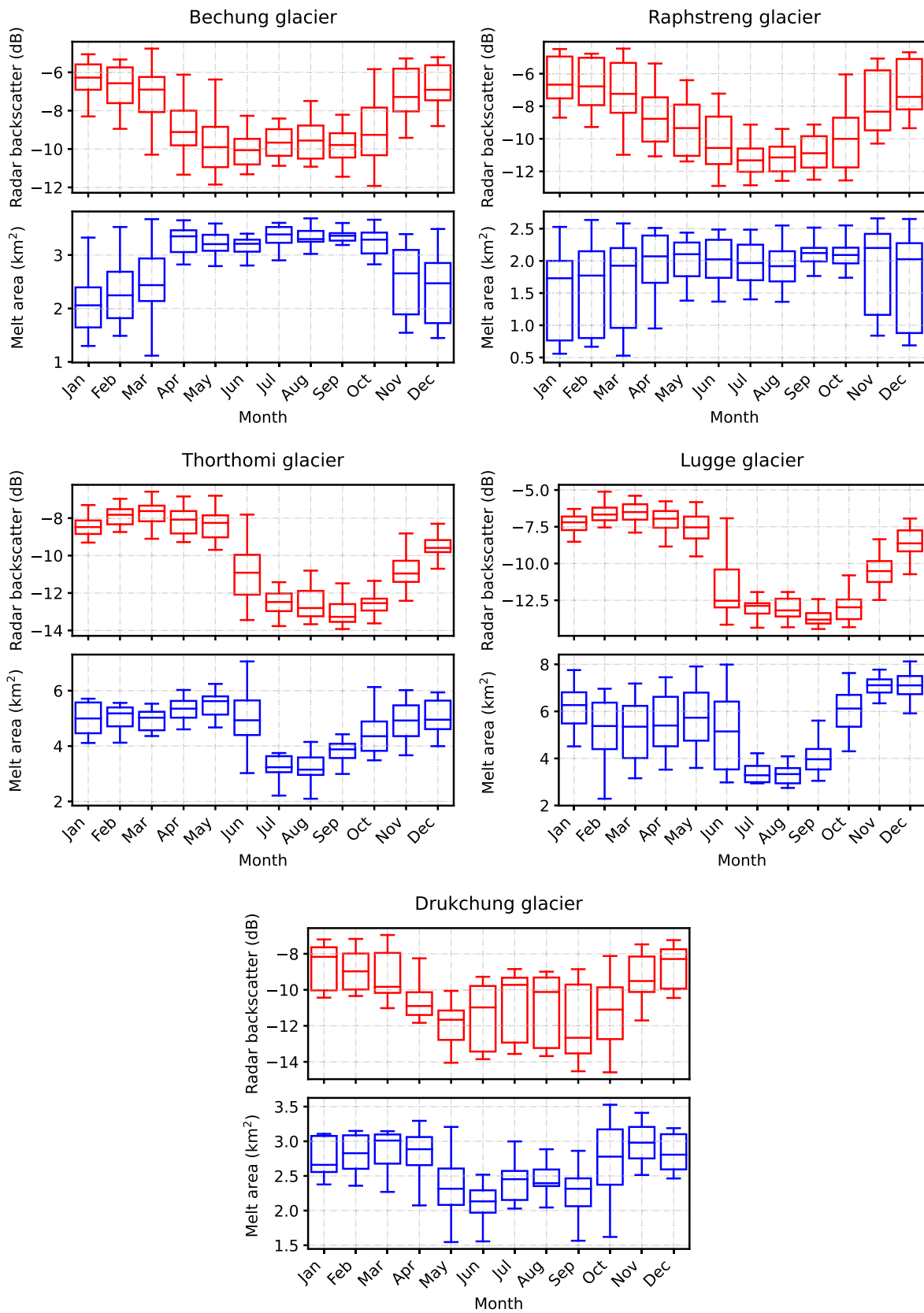
Fig. 7. Monthly variations of the ARBI and glacier melt area. The box length indicates the magnitude of variability of the ARBI and melt area with respect to a month. The horizontal red line within the box represents median value of the ARBI and melt area for each month. The whiskers show the range of variability of the ARBI and melt area for each month.
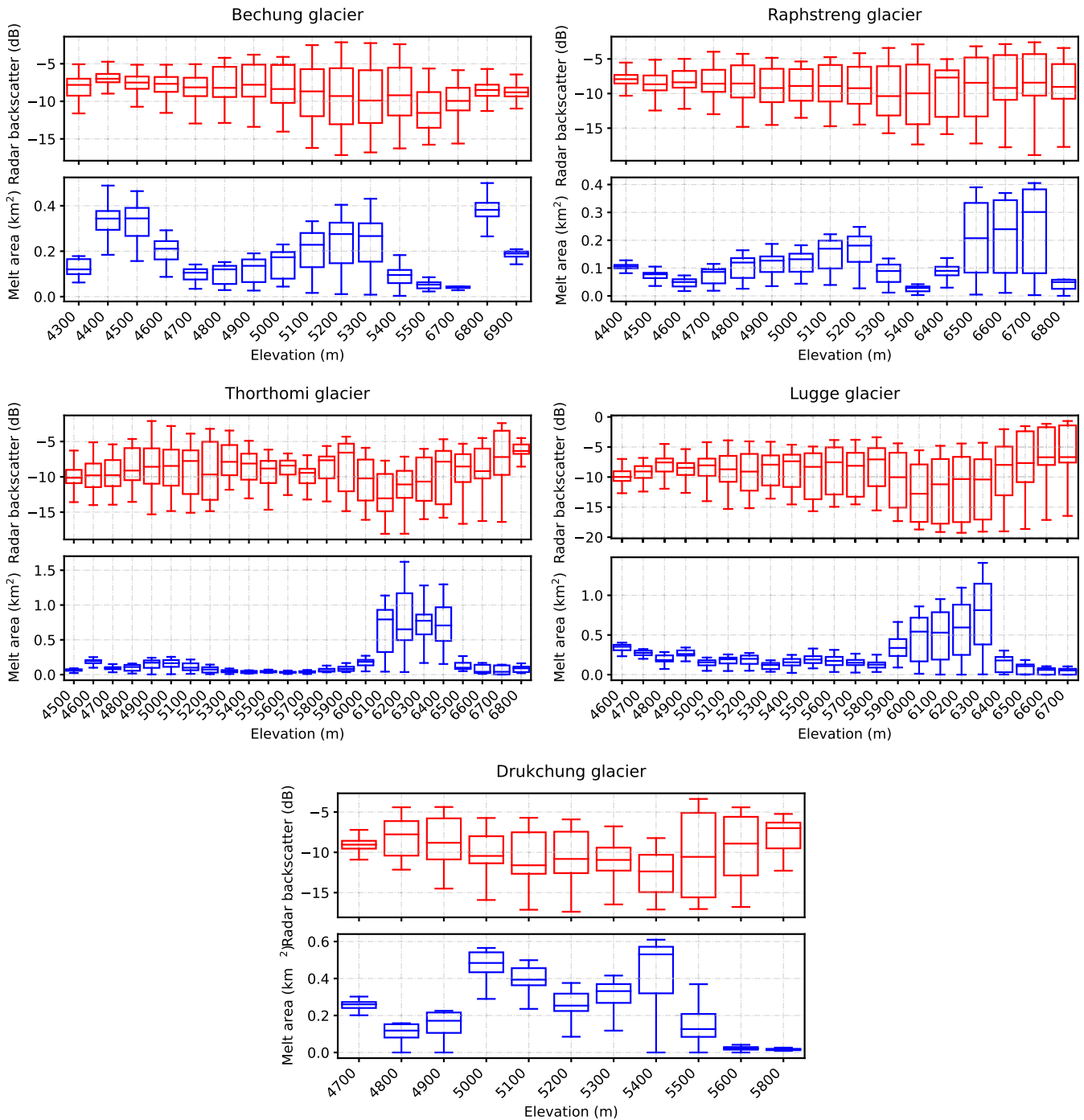
Fig. 8. Variations of the ARBI and glacier melt area with respect to elevations. The box length indicates the magnitude of variability of the ARBI and melt area with respect to elevations. The horizontal red line within the box represents median value of the ARBI and melt area for each elevation bin. The whiskers show the range of variability of the ARBI and melt area for each elevation bin.

downstream, a further investigation is crucial as to understand how the breach occurred and its current and future state. This lake also potentially triggered the deadly 1994 outburst of Lugge Tsho (NCHM, 2019).

5.2. Monitoring glacier melt

For five pro-glacial lakes in Lunana, the Bhutanese Himalayas, their parent glaciers are the main source of water supply and monitoring of these glaciers is crucial. Currently, much effort has been put forward towards monitoring glacier area and length changes and the dataset is freely available for use through GLIMS (Global Land Ice Measurements from Space) initiative (Racoviteanu et al., 2009). The number of studies on the mass balance changes (e.g., Bolch et al., 2008; Shean et al., 2020) and flow velocity (e.g., Dehecq et al., 2015) have also increased in recent decades. Additionally, our findings suggest that the melting statistics of glaciers can be calculated using GEE engine and time-series S-1 SAR data and corroborates the findings of glacier melt in the Bhutanese Himalayas (Scher et al., 2021) (Figs. S2 and S3).

By considering the definition of melting by Baghdadi et al. (1997), glaciers in the region were found to be undergoing melting throughout

Table 6
Projected vertical and horizontal deformation rate and the PSI density at a basin, lake outlet and site (see Fig. 1 for the location of a site).

Sl. no	Feature name	Projected vertical deformation (mm/yr)	Projected horizontal deformation (mm/yr)	Persistent scatterer density (no/km^2)
1	Bechung basin	1.4	–0.34	386
2	Raphstreng basin	1.6	–0.64	266
3	Thorthomi basin	0.57	–0.41	288
4	Lugge basin	–0.06	–1.96	204
5	Drukchung basin	1.28	–0.47	386
6	Bechung outlet	0.78	0.05	356
7	Raphstreng outlet	0.86	–0.21	660
8	Thorthomi outlet	0.5	–0.44	612
9	Lugge outlet	0.7	–0.23	550
10	Drukchung outlet	–2.52	0.23	560
11	Site 1	–0.31	–0.51	341
12	Site 2	–2.47	0.93	793
13	Site 3	–0.32	0.09	10
14	Site 4	–2.73	–3.64	718
15	Site 5	–5.18	–0.35	423

the year and showed contrasting melt behaviour even at a local scale. The contrasting observations were mainly attributed to elevation, area of ablation, and area of accumulation of a glacier (Fig. 11). The ablation region of glaciers (lower elevations) underwent maximum melting compared to accumulation areas. Greater rates of elevation change was also observed in the ablation region (Tsutaki et al., 2019). Our findings suggest that the glacier melt can be controlled by elevation and area of

ablation in addition to debris thickness (Pratap et al., 2015) and pro-glacial lakes (King et al., 2019). The area of glacier ablation and its melting area can be used used as variables for the GLOF susceptibility assessment.

5.3. Monitoring lake basins

Lake basins act as a reservoir for supplying water into a glacial lake. A source of water can be from glaciers and precipitation (snows, hail, rain). Excessive melting of glaciers or a rainstorm within a basin has the potential to trigger lake outbursts by changing hydrostatic pressure of a moraine dam (see Worni et al., 2012). Therefore, Allen et al. (2019) used the size of a basin as one of the parameters for assessing the GLOF susceptibility. In addition to the size of the basin, our findings suggest that the characteristics of the basin such as the contribution from glacier melt and precipitation can be quantified for assessing the GLOF susceptibility (Fig. S4). Basin level backscatter intensity and melt area were found to change seasonally as observed for glaciers due to the melting and freezing of ice and snow surfaces. Therefore, besides considering only the basin area, as per the recommendation by the GAP(2017), including the characteristics of basins into the GLOF susceptibility assessment workflows are recommended.

5.4. Monitoring the stability of moraines and mass movement zones

The stability of moraines and slopes are crucial variables that must be considered for the GLOF susceptibility assessment GAP (2017). The moraine can be composed of ice, rocks, sediments, and soils, and its failure can cause devastating GLOFs (see Clague and Evans, 2000; Richardson and Reynolds, 2000). The entry of mass into a lake in the form of landslide and rock debris can also trigger a GLOF (Byers et al., 2019). Now with the advancement of technology and computing resources, the stability of glacial lake moraines and slopes can be monitored precisely. In our study, all the terminal moraines of lakes were observed to be stable except Drukchung Tsho. The breaching of
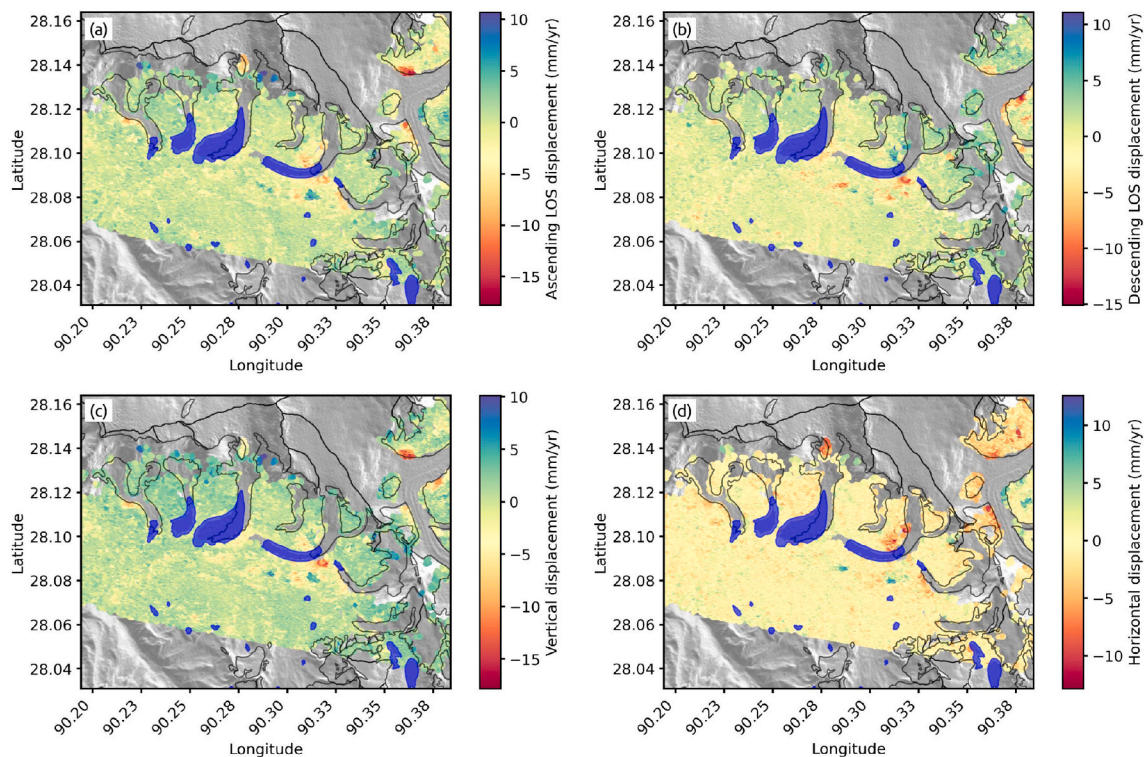

Fig. 9. Example of deformation rate maps, Luanna, the Bhutanese Himalayas. (a) Ascending LOS displacement (mm/yr), (b) descending LOS displacement (mm/yr), (c) projected vertical displacement (mm/yr), and (d) projected horizontal displacement (mm/yr).
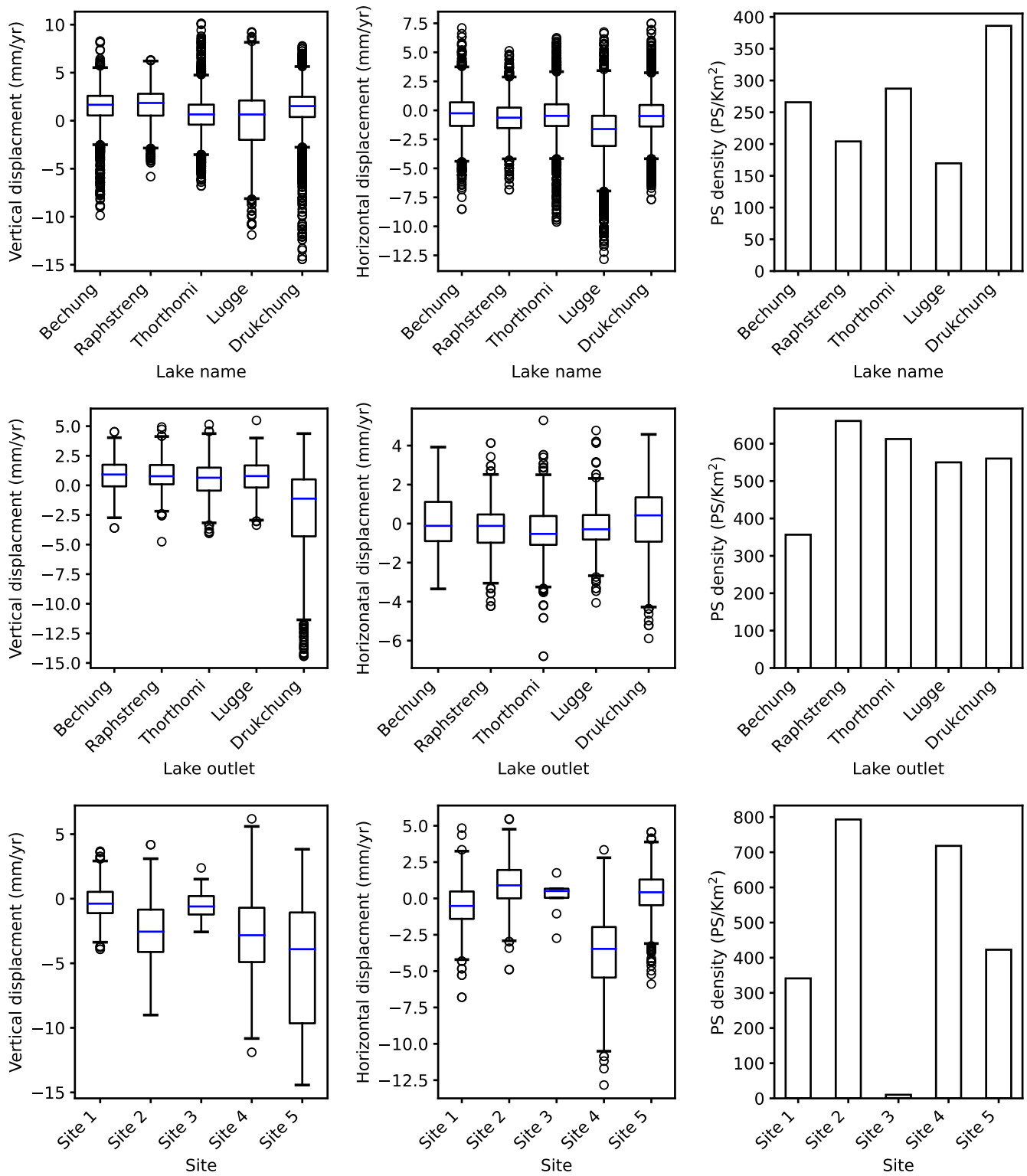
Fig. 10. Projected vertical and horizontal deformation rate and the PSI density at a basin scale (top row), lake outlet (middle row), and site (bottom row). See Fig. 1 for the location of a site. The box plot length indicates the magnitude of variability of the projected deformation at each basin and site within the interquartile range (IQR).The whisker length shows the range of projected deformation in the first and third quartiles and their skewness. The blue line within the box corresponds to the median projected deformation. The persistent scatterers that have undergone a higher magnitude of projected deformation are described as outliers (circles) in the box plot. The bar height corresponds to the number of persistent scatterer density for each basin.
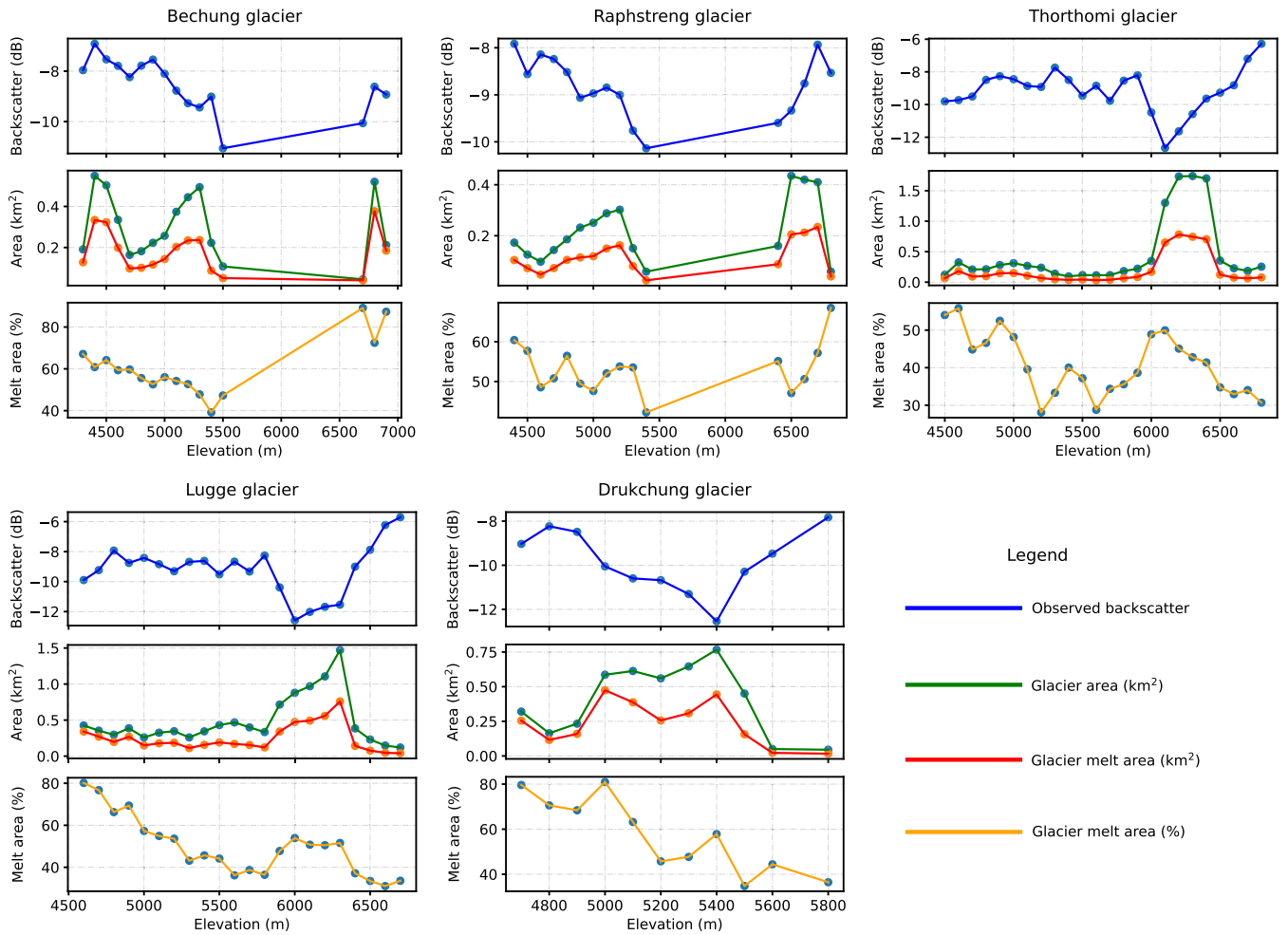
Fig. 11. Average radar backscatter intensity, glacier melt area, and percentage of glacier melt area with respect to elevations. Missing data for Bechung and Raphstreng is due to the absence of glacier-cover on a steep terrain.

Drukchung Tsho around the first week of July 2019 supports our observation well with the instability we observed at the moraine.

We also assessed the stability of lateral moraines and mass movement zones. The thin lateral moraine (~30–45 m wide) that separates Raphstreng and Thorthomi Tsho was observed to be stable in the observation period. The stability of this thin moraine is of huge concern
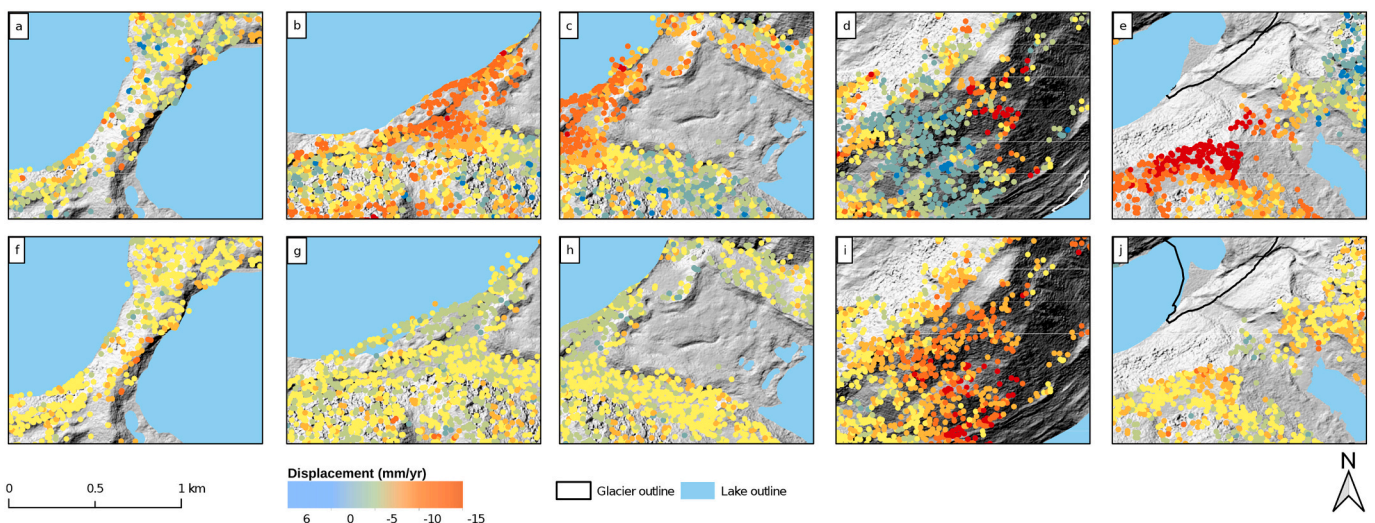

Fig. 12. Projected vertical displacement rate (a, b, c, d, e) and horizontal displacement rate (f, g, h, i, j) of persistent scatterers at site 1, 2, 3, 4, and 5, respectively. See the full description of site in Fig. 1. The background image is a hillshade based on the 2018 SPOT data.

and requires regular monitoring (NCHM, 2019). The lateral moraine of Thorthomi Tsho (site 2, Fig. 12b) was found to be lowering its height (Fig. 12b and g). This suggests that this moraine could contain subsurface ice and therefore requires regular monitoring. The mass movement zone of Lugge Tsho was also found to be moving both horizontally and vertically (site 4, Fig. 12d and i). Analysis of Google Earth images and field photographs taken in 2016 revealed that this site has a rock glacier. Detachment of the rock glacier into the lake could trigger an outburst despite a deadly GLOF in 1994 (Maurer et al., 2020; Fujita et al., 2013; Watanbe and Rothacher, 1996). Therefore, the slope of this lake should be monitored regularly.

5.5. Synthesis of current state of five lakes

Glacial lakes in High Mountain Asia are forming and expanding at an alarming rate (see Chen et al., 2021; Wang et al., 2020) and the Lunana region in the Bhutanese Himalayas, is no exception. Contrasting evolution of glacial lakes even at a local scale is evident in addition to the regional differences in the growth and number of glacial lakes (Gardelle et al., 2011). By integrating FFT, PSI technique and time-series S-1 SAR data within the GEE platform, we showed that glaciers, glacial lakes and their surroundings can be regularly monitored in detail, which is a huge improvement compared to existing methods. While we found that one interferometric pair per month provided sufficient data to study multi-year deformation trends, other studies may benefit from performing PSI on denser temporal stacks of imagery which would allow seasonal deformation trends to be identified. From the time-series S-1 SAR data of the lake area of Raphstrng Tsho, it was clear that the lake has attained its maximum growth. The detachment of the lake from its parent glacier can be expected within a decade. Compared to the surrounding lakes, the lake seems to be quite deep, consistent with a maximum depth of 110 m (NCHM, 2019). The lack of regular pattern of highs and lows in the ARBI and open water area variations supports this observation. Therefore, this lake could be still dangerous during winter, where S-1 SAR data can be used for monitoring this lake all year round. The terminal moraines and mass movement zones were likely stable during the observation period as the projected vertical and horizontal components of movements were within the range of sensitivity of the PSI technique (Fig. 10). Avalanche-prone areas could not be monitored using the PSI technique due to the decorrelation of signals. In the decorrelated areas such as over a glacier surface and the terminal moraine of Lugge Tsho (Fig. 4e and i), a significant surface lowering can be seen in the DEM differencing results. In the PSI maps, there are no persistent scatterers on the glacier surfaces and only a few on the terminal moraine of Lugge Tsho, indicating the presence of subsurface ice for the latter (Fig. 12c and h). Therefore, our study confirms the suitability of the PSI technique for monitoring the stability of slopes and moraines.

Thorthomi Tsho shows a completely different evolutionary path. Icebergs are common on the lake surface thereby preventing the application of semi-automated and automated approaches (Wangchuk and Bolch, 2020). However, we confirmed that the time-series S-1 SAR backscatter intensity data can be used to monitor its open water area variations automatically. An abnormal increase in the open water area should be interpreted as an active melting and displacement of icebergs. An effort should be put forward to monitor this lake owing to its size (4.4 km^2) and the thin lateral moraine that separates from Raphstreng Tsho. Although significant subsidence was not observed on this moraine (site 1), it should be still closely monitored for its vulnerabilities. Its failure would release large amounts of water into the Raphstreng Tsho triggering a chain of catastrophic floods. Additionally, the southeast lateral moraine (site 2) showed considerable subsidence and appeared to contain ice. These findings suggest that this lake is still highly dangerous despite the mitigation work carried out between 2008 and 2012 (Singh, 2009) and a partial outburst in 2019 (Kuensel, 2019).

Time-series S-1 SAR data on Lugge Tsho revealed that the lake might

not be as deep as Raphstreng Tsho as it underwent seasonal changes in its state. Its seasonal changes in the radar backscatter intensity and open water area were comparable to Bechung Tsho. Lugge Tsho was previously recorded as having a partial outburst in 1994 (Maurer et al., 2020) with a flood volume of 17 million cubic meters (Fujita et al., 2008). Another outburst from Lugge Tsho is very likely if those actively moving sidewalls (site 4 and 5) detach into the lake and generate enough tsunami-like waves to trigger an outburst. Additionally, partial drainage of Drukchung Tsho in 2019 would have supplied additional water into Lugge Tsho and changed its hydrostatic pressure regime. A further investigation on the interaction between Lugge Tsho and Drukchung Tsho is thus required.

Bechung Tsho is a recently formed proglacial lake and the fastest expanding lake in the region. The terminal moraine was likely stable as the deformation rate was in the range of the PSI sensitivity. The low density of persistent scatterers, compared to the neighbouring terminal moraines, could be due to the encroachment of vegetation at its moraine as the presence of vegetation decorrelates the C-band signal. Although lake expansion alone is not necessarily a sign of danger (Watanabe et al., 2009), a combination of extreme lake expansion and glacier melt might compromise the moraine. Therefore, continuous monitoring of this lake is also highly recommended.

6. Conclusions

Glacial lakes pose a serious threat in many mountainous parts of the world, and as such regular monitoring is needed to detect any changes that could signify instabilities. Yet challenges remains in monitoring glacial lakes with available optical satellites (e.g., Landsat, Sentinel-2) as they lack cloud penetrating capabilities. In this study, we demonstrated the integration of techniques and the use of a time-series of Sentinel-1 SAR (S-1 SAR) data, the Google Earth Engine (GEE) platform, and Persistent Scatterer Interferometry (PSI) techniques to achieve the objective. We showed the capability of the time-series S-1 SAR backscatter data to monitor glaciers, basins, and glacial lakes in the Lunana region of the Bhutanese Himalayas. Glaciers, basins, and glacial lakes can be monitored by studying their radar backscatter intensity changes. The radar backscatter information can be interpreted to determine the statistics of glacier melt and the periodicity of freezing and thawing of glaciers and glacial lakes. All the glaciers and basins in the region showed periodicity in their ARBI with a repeat cycle of 359–365 days. All glacial lakes except Raphstreng Tsho and Drukchung Tsho showed seasonal change in their ARBI and freezing and thawing patterns. Using a radar backscatter intensity information, open water area, ice area, and the duration of glacial lake ice formation can be calculated.

The study also demonstrated the suitability of using the PSI technique for monitoring the stability of moraine dam and mass movement zones of a lake. Using the technique we found the terminal moraine of Drukchung Tsho unstable. It showed a projected vertical deformation rate of –2.52 mm/yr. The breaching of the terminal moraine of Drukchung Tsho around the first week of July 2019 correlated well with the instability detected by the PSI technique. We also found the lateral moraine of Thorthomi Tsho (site 2) and the slope of Lugge Tsho (site 4) unstable. Both showed a projected vertical deformation rate of –2.47 mm/yr and –2.73 mm/yr respectively. Therefore, both the lateral moraine and slope require regular monitoring which can be facilitated by our approach.

Since the tools, techniques and datasets are freely available, our integrated approach is well applicable to any other region on earth. This allows continuous monitoring of glacial lakes and their outburst susceptibility can be detected in a timely manner.

7. Methodology and results reproducibility

All datasets and codes (Python and JavaScript) used for data analysis and visualization are openly available at my GitHub and GEE repository.

In addition, an updated snap2stamps package which now supports Python 3 (snap2stampspy3) and multi-swath processing of Sentinel-1 data is also available. The manual and script for decomposing LOS displacement into vertical and horizontal component is available only upon request. The following datasets, tools, and software were used to conduct this study: Copernicus Sentinel-1 and -2, SRTM DEM, Python, SNAP, StaMPS, MATLAB, Linux OS, GitHub, Inkscape, QGIS, and GEE which are all open source except MATLAB.

CRediT authorship contribution statement

Sonam Wangchuk: Conceptualization, Methodology, Software, Validation, Formal analysis, Investigation, Data curation, Writing – original draft, Visualization, Funding acquisition. **Tobias Bolch:** Conceptualisation, Methodology, Resources, Supervision, Writing – review & editing, Project administration, Funding acquisition. **Benjamin Aubrey Robson:** Resources, Methodology, Writing – review & editing.

Declaration of Competing Interest

The authors declare that they have no known competing financial interests or personal relationships that could have appeared to influence the work reported in this paper.

Acknowledgements

Appendix A. Supplementary data

Supplementary data to this article can be found online at https://doi.org/10.1016/j.rse.2022.112910.

References

Allen, S.K., Zhang, G., Wang, W., Yao, T., Bolch, T., 2019. Potentially dangerous glacial lakes across the Tibetan Plateau revealed using a large-scale automated assessment approach. Sci. Bulletin 64 (7), 435–445.

Baghdadi, N., Gauthier, Y., Bernier, M., 1997. Capability of multitemporal ERS-1 SAR data for wet-snow mapping. Remote Sens. Environ. 60 (2), 174–186.

Bekaert, D., Walters, R., Wright, T., Hooper, A., Parker, D., 2015. Statistical comparison of insar tropospheric correction techniques. Remote Sens. Environ. 170, 40–47.

Blasco, J.D., Foumelis, M., Stewart, C., Hooper, A., 2019. Measuring urban subsidence in the rome metropolitan area (Italy) with Sentinel-1 snap-stamps persistent scatterer interferometry. Remote Sens. 11 (2), 129.

Bolch, T., Buchroithner, M.F., Pieczonka, T., Kunert, A., 2008. Planimetric and volumetric glacier changes in the Khumbu Himal, Nepal, since 1962 using Corona, Landsat TM and ASTER data. J. Glaciol. 54 (187), 592–600.

Bolch, T., Peters, J., Yegorov, A., Pradhan, B., Buchroithner, M., Blagoveshchensky, V., 2011. Identification of potentially dangerous glacial lakes in the Northern Tien Shan. Nat. Hazards 59 (3), 1691–1714.

Byers, A.C., Rounce, D.R., Shugar, D.H., Lala, J.M., Byers, E.A., Regmi, D., 2019. A rockfall-induced glacial lake outburst flood, upper barun valley, Nepal. Landslides 16 (3), 533–549.

Carrivick, J.L., Tweed, F.S., 2016. A global assessment of the societal impacts of glacier outburst floods. Glob. Planet. Change 144, 1–16.

Clague, J.J., Evans, S.G., 2000. A review of catastrophic drainage of moraine-dammed lakes in British Columbia. Quat. Sci. Rev. 19 (17-18), 1763–1783.

Cook, S.J., Kougkoulos, I., Edwards, L.A., Dortch, J., Hoffmann, D., 2016. Glacier change and glacial lake outburst flood risk in the bolivian andes. Cryosphere 10 (5), 2399–2413.

Dini, B., Manconi, A., Loew, S., 2019. Investigation of slope instabilities in NW Bhutan as derived from systematic dinsar analyses. Eng. Geol. 259, 105111.

Fattahi, H., Agram, P., Simons, M., 2016. A network-based enhanced spectral diversity approach for tops time-series analysis. IEEE Trans. Geosci. Remote Sens. 55 (2), 777–786.

Foumelis, M., 2018. Vector-based approach for combining ascending and descending persistent scatterers interferometric point measurements. Geocarto Int. 33 (1), 38–52.

Fujita, K., Sakai, A., Takenaka, S., Nuimura, T., Surazakov, A., Sawagaki, T., Yamanokuchi, T., 2013. Potential flood volume of Himalayan glacial lakes. Nat. Hazards Earth Sys. Sci. 13 (7), 1827–1839.

Fujita, K., Suzuki, R., Nuimura, T., Sakai, A., 2008. Performance of ASTER and SRTM DEMs, and their potential for assessing glacial lakes in the Lunana region, Bhutan Himalaya. J. Glaciol. 54 (185), 220–228.

GAPHAZ2017, 2017. Assessment of glacier and permafrost hazards in mountain regions - technical guidance document. prepared by Allen, s., Frey, h., Huggel, c. et al. Report 72. In: Standing Group on Glacier and Permafrost Hazards in Mountains (GAPHAZ) of the International Association of Cryospheric Sciences (IACS) and the International Permafrost Association (IPA). Zurich, Switzerland / Lima, Peru.

Gardelle, J., Arnaud, Y., Berthier, E., 2011. Contrasted evolution of glacial lakes along the Hindu Kush Himalaya Mountain range between 1990 and 2009. Glob. Planet. Change 75 (1-2), 47–55.

Gardelle, J., Berthier, E., Arnaud, Y., Kääb, A., 2013. Region-wide glacier mass balances over the Pamir-Karakoram-Himalaya during 1999–2011. Cryosphere 7 (4), 1263–1286.

Gorelick, N., Hancher, M., Dixon, M., Ilyushchenko, S., Thau, D., Moore, R., 2017. Google Earth engine: planetary-scale geospatial analysis for everyone. Remote Sens. Environ. 202, 18–27.

Gurung, D.R., Khanal, N.R., Bajracharya, S.R., Tsering, K., Joshi, S., Tshering, P., Chhetri, L.K., Lotay, Y., Penjor, T., 2017. Lemthang tsho glacial lake outburst flood (glof) in Bhutan: cause and impact. Geoenviron. Disasters 4 (1), 1–13.

Harrison, S., Kargel, J.S., Huggel, C., Reynolds, J., Shugar, D.H., Betts, R.A., Emmer, A., Glasser, N., Haritashya, U.K., Klimes, J., et al., 2018. Climate change and the global pattern of moraine-dammed glacial lake outburst floods. Cryosphere 12 (2), 1195–1209.

Hirschmüller, H., 2011. Semi-global matching-motivation, developments and applications. Photogramm. Week 11, 173–184.

Hooper, A., Bekaert, D., Spaans, K., Arikan, M., 2012. Recent advances in SAR interferometry time series analysis for measuring crustal deformation. Tectonophysics 514, 1–13.

How, P., Messerli, A., Mätzler, E., Santoro, M., Wiesmann, A., Caduff, R., Langley, K., Bojesen, M.H., Paul, F., Kääb, A., et al., 2021. Greenland-wide inventory of ice marginal lakes using a multi-method approach. Sci. Rep. 11 (1), 1–13.

Huggel, C., Kääb, A., Haeberli, W., Teysseire, P., Paul, F., 2002. Remote sensing based assessment of hazards from glacier lake outbursts: a case study in the Swiss Alps. Can. Geotech. J. 39 (2), 316–330.

Kargel, J.S., Leonard, G.J., Shugar, D.H., Haritashya, U.K., Bevington, A., Fielding, E., Fujita, K., Geertsema, M., Miles, E., Steiner, J., et al., 2016. Geomorphic and geologic controls of geohazards induced by Nepal's 2015 Gorkha Earthquake. Science 351 (6269).

King, O., Bhattacharya, A., Bhambri, R., Bolch, T., 2019. Glacial lakes exacerbate Himalayan glacier mass loss. Sci. Rep. 9 (1), 1–9.

Komori, J., 2008. Recent expansions of glacial lakes in the Bhutan Himalayas. Quart. Int. 184 (1), 177–186.

Kuensel, 2019. Heat Wave and Delayed Monsoon Caused Thorthormi to Breach. https://kuenselonline.com/heat-wave-and-delayed-monsoon-caused-thorthormi-to-breach/. . Accessed 03 Onctober 2021.

Mahagaonkar, A., Wangchuk, S., Ramanathan, A., Tshering, D., Mahanta, C., 2017. Glacier environment and climate change in Bhutan-an overview. J. Clim. Change 3 (2), 1–10.

Maurer, J., Schaefer, J., Russell, J., Rupper, S., Wangdi, N., Putnam, A., Young, N., 2020. Seismic observations, numerical modeling, and geomorphic analysis of a glacier lake outburst flood in the Himalayas. Sci. Adv. 6 (38), eaba3645.

McKillop, R.J., Clague, J., 2007. Statistical, remote sensing-based approach for estimating the probability of catastrophic drainage from moraine-dammed lakes in Southwestern British Columbia. Glob. Planet. Change 56 (1-2), 153–171.

Miles, K.E., Willis, I.C., Benedek, C.L., Williamson, A.G., Tedesco, M., 2017. Toward monitoring surface and subsurface lakes on the Greenland ice sheet using Sentinel-1 SAR and Landsat-8 OLI imagery. Front. Earth Sci. 5, 58.

Nagai, H., Fujita, K., Sakai, A., Nuimura, T., Tadono, T., 2016. Comparison of multiple glacier inventories with a new inventory derived from high-resolution alos imagery in the Bhutan Himalaya. Cryosphere 10 (1), 65–85.

Nagai, H., Ukita, J., Narama, C., Fujita, K., Sakai, A., Tadono, T., Yamanokuchi, T., Tomiyama, N., 2017. Evaluating the scale and potential of glof in the Bhutan Himalayas using a satellite-based integral glacier-glacial lake inventory. Geosciences 7 (3), 77.

Narama, C., Duishonakunov, M., Kääb, A., Daiyrov, M., Abdrakhmatov, K., 2010. The 24 july 2008 outburst flood at the Western Zyndan glacier lake and recent regional changes in glacier lakes of the Teskey ala-too Range, Tien Shan, Kyrgyzstan. Nat. Hazards Earth Sys. Sci. 10 (4), 647–659.

NCHM, 2019. Reassessment of Potentially Dangerous Glacial Lakes In Bhutan. Prepared By Cryosphere Services Division, NCHM. Report 40. National Center for Hydrology and Meteorology, Royal Government of Bhutan PO Box: 2017, Thimphu, Bhutan.

Nuimura, T., Sakai, A., Taniguchi, K., Nagai, H., Lamsal, D., Tsutaki, S., Kozawa, A., Hoshina, Y., Takenaka, S., Omiya, S., et al., 2015. The gamdam glacier inventory: a quality-controlled inventory of Asian glaciers. Cryosphere 9 (3), 849–864.

Nuth, C., Kääb, A., 2011. Co-registration and bias corrections of satellite elevation data sets for quantifying glacier thickness change. Cryosphere 5 (1), 271–290.

Partington, K., 1998. Discrimination of glacier facies using multi-temporal SAR data. J. Glaciol. 44 (146), 42–53.

Petrov, M.A., Sabitov, T.Y., Tomashevskaya, I.G., Glazirin, G.E., Chernomorets, S.S., Savernyuk, E.A., Tutubalina, O.V., Petrakov, D.A., Sokolov, L.S., Dokukin, M.D., et al., 2017. Glacial lake inventory and lake outburst potential in Uzbekistan. Sci. Total Environ. 592, 228–242.

Pratap, B., Dobhal, D., Mehta, M., Bhambri, R., 2015. Influence of debris cover and altitude on glacier surface melting: a case study on Dokriani glacier, central Himalaya, India. Annals Glaciol. 56 (70), 9–16.

Racoviteanu, A.E., Paul, F., Raup, B., Khalsa, S.J.S., Armstrong, R., 2009. Challenges and recommendations in mapping of glacier parameters from space: results of the 2008 global land ice measurements from space (glims) workshop, boulder, Colorado, USA. Annals Glaciol. 50 (53), 53–69.

Richardson, S.D., Reynolds, J.M., 2000. An overview of glacial hazards in the Himalayas. Quart. Int. 65, 31–47.

Rounce, D.R., McKinney, D.C., Lala, J.M., Byers, A.C., Watson, C.S., 2016. A new remote hazard and risk assessment framework for glacial lakes in the Nepal Himalaya. Hydrol. Earth Sys. 20 (9), 3455.

Scapozza, C., Ambrosi, C., Cannata, M., Strozzi, T., 2019. Glacial lake outburst flood hazard assessment by satellite earth observation in the Himalayas (chomolhari area, Bhutan). Geograph. Helv. 74 (1), 125–139.

Scher, C., Steiner, N.C., McDonald, K.C., 2021. Mapping seasonal glacier melt across the Hindu Kush Himalaya with time series synthetic aperture radar (SAR). Cryosphere 15, 4465–4482.

Shean, D.E., Bhushan, S., Montesano, P., Rounce, D.R., Arendt, A., Osmanoglu, B., 2020. A systematic, regional assessment of high mountain Asia glacier mass balance. Frontiers in Earth Science 7, 363.

Shugar, D.H., Burr, A., Haritashya, U.K., Kargel, J.S., Watson, C.S., Kennedy, M.C., Bevington, A.R., Betts, R.A., Harrison, S., Strattman, K., 2020. Rapid worldwide growth of glacial lakes since 1990. Nat. Clim. Change 10 (10), 939–945.

Singh, S.M., 2009. The Cost of Climate Change: The Story Of Thorthormi Glacial Lake In Bhutan. Report 39. World Wide Fund for Nature, Thimphu, New Delhi, Kathmandu.

Strozzi, T., Wiesmann, A., Kääb, A., Joshi, S., Mool, P., 2012. Glacial lake mapping with very high resolution satellite SAR data. Nat. Hazards Earth Sys. Sci. 12 (8.), 2487–2498.

Tofani, V., Raspini, F., Catani, F., Casagli, N., 2013. Persistent scatterer interferometry (psi) technique for landslide characterization and monitoring. Remote Sens. 5 (3), 1045–1065.

Tsutaki, S., Fujita, K., Nuimura, T., Sakai, A., Sugiyama, S., Komori, J., Tshering, P., 2019. Contrasting thinning patterns between lake-and land-terminating glaciers in the Bhutanese Himalaya. Cryosphere 13 (10), 2733–2750.

Tukey, J.W., et al., 1977. Exploratory data analysis. Addison-Wesley. Reading, Massachusetts, Menlo Park, California, London, Amsterdam, Don Mills, Ontario, Sydney.

Veh, G., Korup, O., von Specht, S., Roessner, S., Walz, A., 2019. Unchanged frequency of moraine-dammed glacial lake outburst floods in the Himalaya. Nat. Clim. Change 9 (5), 379–383.

Wang, W., Yao, T., Yang, W., Joswiak, D., Zhu, M., 2012. Methods for assessing regional glacial lake variation and hazard in the southeastern tibetan plateau: a case study from the Boshula mountain range, China. Environ. Earth Sci. 67 (5), 1441–1450.

Wang, X., Guo, X., Yang, C., Liu, Q., Wei, J., Zhang, Y., Liu, S., Zhang, Y., Jiang, Z., Tang, Z., 2020. Glacial lake inventory of high-mountain Asia in 1990 and 2018 derived from landsat images. Earth Sys. Sci. Data 12 (3), 2169–2182.

Wangchuk, S., Bolch, T., 2020. Mapping of glacial lakes using Sentinel-1 and Sentinel-2 data and a random forest classifier: strengths and challenges. Sci. Remote Sens. 2, 100008.

Wangchuk, S., Bolch, T., Zawadzki, J., 2019. Towards automated mapping and monitoring of potentially dangerous glacial lakes in Bhutan Himalaya using Sentinel-1 synthetic Aperture radar data. Int. J. Remote Sens. 40 (12), 4642–4667.

Watanabe, T., Lamsal, D., Ives, J.D., 2009. Evaluating the growth characteristics of a glacial lake and its degree of danger of outburst flooding: imja Glacier, Khumbu Himal Nepal. Norsk Geografisk Tidsskrift-Norwegian J. Geograph. 63 (4), 255–267.

Watanbe, T., Rothacher, D., 1996. The 1994 lugge TSHO glacial lake outburst flood, Bhutan Himalaya. Mountain Res. Dev. 16 (1), 77–81.

Westoby, M.J., Glasser, N.F., Brasington, J., Hambrey, M.J., Quincey, D.J., Reynolds, J. M., 2014. Modelling outburst floods from moraine-dammed glacial lakes. Earth-Sci. Rev. 134, 137–159.

Wilson, R., Harrison, S., Reynolds, J., Hubbard, A., Glasser, N.F., Wündrich, O., Anacona, P.I., Mao, L., Shannon, S., 2019. The 2015 chileno valley glacial lake outburst flood, Patagonia. Geomorphology 332, 51–65.

Worni, R., Stoffel, M., Huggel, C., Volz, C., Casteller, A., Luckman, B., 2012. Analysis and dynamic modeling of a moraine failure and glacier lake outburst flood at ventisquero negro, patagonian andes (Argentina). J. Hydrol. 444, 134–145.

Zhang, G., Yao, T., Xie, H., Wang, W., Yang, W., 2015. An inventory of glacial lakes in the third Pole region and their changes in response to global warming. Glob. Planet. Change 131, 148–157.

Zhang, Y., Zhang, G., Zhu, T., 2020. Seasonal cycles of lakes on the Tibetan plateau detected by Sentinel-1 SAR data. Sci. Total Environ. 703, 135563.

Zheng, G., Mergili, M., Emmer, A., Allen, S., Bao, A., Guo, H., Stoffel, M., 2021. The 2020 glacial lake outburst flood at Jinwuco, Tibet: causes, impacts, and implications for hazard and risk assessment. Cryosphere 15, 3159–3180.

Dussaillant, Alejandro, et al., 2010. Repeated glacial-lake outburst floods in patag -onia: an increasing hazard? Nat. Hazards 54 (2), 469–481.

Kropacek, J., et al., 2015. Repeated glacial lake outburst flood threatening the oldest Buddhist monastery in North-Western Nepal. Nat. Hazards Earth Sys. Sci. 15 (10), 2425–2437.

Dehecq, A., Gourmelen, N., Trouvé, E., 2015. Deriving large scale glacier velocities from a complete satellite archive: application to the Pamir-Karakoram -Himalaya. Remote Sens. Environ. 162, 55–66.

Chen, F., et al., 2021. Annual 30 m dataset for glacial lakes in high mountain Asia from 2008 to 2017. Earth Sys. Sci. Data 13 (2), 741–766.